

The Double Cluster

by Eva Gmelich Meijling

In memory of my dad,
Jan Gmelich Meijling

You will forever be in the starshine of my night.

Cover image: A colour image of the Double Cluster, NGC869 and NGC884.

Image acquisition: Obtained at the Anton Pannekoek Observatory at the UvA by Eva Gmelich Meijling using a 51 cm telescope with FLI Pro-Line 16803 CCD camera. The total exposure time was 2 hours and 7 minutes in the BVR broadband filters.

Image processing: Processed in MaximDL and Adobe Photoshop by Rasjied Sloot.

Thesis word count: 6418 words

Sterrenclusters zijn hoopjes met sterren die tegelijkertijd zijn ontstaan. Door de kleur en helderheid van deze sterren te meten kan de afstand en leeftijd van de cluster worden bepaald.

In dit onderzoek heb ik twee bijzondere clusters geobserveerd in het sterrenbeeld Perseus: h en χ Persei. Aangezien deze twee clusters dicht bij elkaar in de buurt staan aan de hemel, heten ze gezamenlijk ‘het dubbelcluster’. Ik vroeg mij af of deze twee clusters uit hetzelfde stervormingsgebied zijn geboren.

Om dit te onderzoeken, heb ik op de nacht van 13 op 14 juni 2021 door middel van een hele grote telescoop (zie afbeelding 1) op het Anton Pannekoek Observatorium in Amsterdam-Oost deze dubbelcluster waargenomen. Met deze telescoop heb ik verschillende foto’s met hele lange belichtingstijden (tot wel 60 seconden) gemaakt. Door deze foto’s na afloop met elkaar te combineren heb ik de informatie die ik nodig heb voor mijn onderzoek verzameld.



Afbeelding 1

Door de helderheid en kleur van bijna 10 duizend sterren te meten aan de hand van deze foto’s, heb ik een leeftijd en afstand van beiden clusters kunnen berekenen. Het resultaat? Ze staan ongeveer 8000 lichtjaar ver weg, en zijn tussen 20 en 40 miljoen jaar oud!

De conclusie die ik uit mijn resultaten heb kunnen trekken is dat het mogelijk is dat h Persei een zusje is van χ Persei.



Afbeelding 2. Deze telescopen zijn niet gebruikt voor het onderzoek. Wel zijn ze deel van het Anton Pannekoek Observatorium.

Contents

1	Introduction	2
1.1	Motivation and goal of study	3
2	Theoretical background	3
2.1	Open cluster formation and morphology	3
2.2	Stellar evolution and zero age main sequence	3
2.3	Cluster membership and field stars	4
2.4	Reddening and distance modulus	4
2.5	Cluster age and turnoff point	4
3	Observations	5
3.1	Target selection criteria	5
3.1.1	The Double Cluster (NGC869 and NGC884)	5
3.1.2	Considerations for the Double Cluster (NGC869 and NGC884)	5
3.2	Observing runs	5
3.2.1	March 3 rd 2021 at Rasjied's Observatory	5
3.2.2	April 16 th 2021 at Anton Pannekoek Observatory, Small Dome	5
3.2.3	June 13 th 2021 at Anton Pannekoek Observatory, Big Dome	5
3.3	Data reduction	6
3.3.1	Pre-processing	6
3.3.2	Plate solving	6
4	Analysis	6
4.1	Data processing	6
4.2	Aperture photometry	7
4.3	Cleaning up initial data set	9
4.3.1	Filter long and short exposure times	9
4.3.2	Filter on low SNR and duplicates from overlapping planes	9
4.4	Position of measured stars	9
4.4.1	Angular distance to cluster centre	9
4.4.2	Distance to Earth	10
4.5	Main sequence fitting	10
4.5.1	Dereddening, extinction and distance	11
4.5.2	Cluster age	12
5	Results and discussion	12
5.1	The distances to NGC869 and NGC884	12
5.2	The ages of NGC869 and NGC884	14
6	Conclusions	14
6.1	Suggestions for future work	14
A	Background subtraction and Starfinder	16
B	Aperture photometry: aperture radius	17
C	Determination of the cluster centre	18
D	Core and halo population	19
E	3D plot of the Double Cluster	20
F	Colour-magnitude diagrams	21
G	CMDs without selection based on distance	22
H	NGC884	23
I	Observing logs	25

Siblings or strangers; Determining the distance and age of the Double Cluster h and χ Persei

Bachelor Thesis

Eva C.V. Gmelich Meijling

Email: evameijling@gmail.com
Amsterdam University College
Tutor: Ydwine Zanstra
Student Nr. 12162124
Major: Sciences

Supervisor: Drs. M.R. Sloot¹
Email: m.r.sloot@uva.nl

2nd Reader: Prof. dr. R.A.D. Wijnands¹
Email: r.a.d.wijnands@uva.nl

¹ Anton Pannekoek Institute for Astronomy, University of Amsterdam

Received December 22, 2021

ABSTRACT

Historically, membership selection of cluster stars was based just on stellar distribution visible in the observed plane. Ever since satellites measure parallaxes, physical distances to stars can be included as a parameter.

The two open clusters h and χ Persei are interesting celestial bodies to compare due to their similar distance to Earth and mutual proximity. The aim of this study is to determine the distance and age of these clusters, exploring the possibility of a single epoch of stellar formation.

Four planes were obtained with the 51 cm telescope at the Anton Pannekoek Observatory in Amsterdam. By enhancing this photometric data with parallax measurements from the Gaia Data Release 3, the number of field stars in the cluster's planes were reduced. The distance to h and χ Persei is determined by using a zero age main sequence fit on both clusters, taking interstellar reddening and extinction effects into consideration. The ages of the clusters are found through direct comparison of the stars in the clusters' colour-magnitude diagrams with varying isochrones.

I found that both clusters share a similar age of 20-40 Myr. The distances found for h and χ Persei are 2565^{+85}_{-90} pc and 2380^{+70}_{-75} pc, respectively.

Although varying distances and similar ages were found for both clusters, a single epoch of stellar formation cannot be ruled out since their mutual distance of 185 ± 110 pc is not much larger than the typical size of a molecular cloud from which they could have been formed.

Key words. open clusters and associations: individual (NGC869, NGC884) – Double Cluster – stellar evolution models – photometry – age and distance determination – Gaia parallaxes

1. Introduction

At the start of the Common Era, astronomer and mathematician Ptolemy introduced the idea of heavenly bodies attached to nested spheres. The movement of stars was thought to originate from the outermost revolving sphere. This theory was generally adopted until Nicholas Copernicus in 1542 suspected the stars to be located at varying distances from Earth. By measuring the parallax of 61 Cygni in 1838 with a heliometer, German

astronomer Friedrich Wilhelm Bessel was able to provide proof for this belief (Jones 2020).

Nowadays, we have satellites to measure the parallaxes of celestial bodies. The Hipparchus satellite, launched in 1989, was the first to make such measurements with milliarcsecond precision. In 2013, the European Space Agency launched the Gaia satellite which can measure parallax angles up to an accuracy of 10 microarcseconds (Bailer-Jones 2004). This means that for stars at 2.5 kpc distance, the uncertainty is ± 60 pc.

When looking at the night sky, Ptolemy's theory does not seem so bizarre; stars appear to have fixed positions under a rotation Earth. In reality, the celestial objects you see at the night's sky span very different distances. In high density stellar regions named open clusters stars do roughly have the same distance to Earth. Their similar distances to Earth offer the opportunity to study their true variety in luminosity. By examining these luminosities with the naked eye, one can approximate the age of the cluster. The presence of bright white-bluish stars implies a young cluster where massive stars are still burning hydrogen in their cores. Examining these luminosities in photometric bands with high precision will reveal clues to when and how these objects formed.

1.1. Motivation and goal of study

By determining the distance and age of stars in open clusters, more knowledge is attained with regard to stellar formation and cluster membership. Open clusters offer insight in the evolution of massive stars, which are rare in the universe.

My personal motivation for this project is to acquire knowledge and skills that are required to independently observe stellar objects, process the corresponding data and adequately analyse it.

The research question of this study is: *Can h and χ Persei originate from the same molecular cloud?* To answer this question this study investigates the distance and age of the Double Cluster, consisting of h and χ Persei, through photometric observations at the Anton Pannekoek Observatory and astrometric data collected from the Gaia satellite. This study will mainly focus on the observations and the optimisation of the imaging and analysis techniques.

The structure of this thesis is as follows: section 2 elucidates important theoretical concepts required for understanding the analysis. A detailed description of the observational aspect of the research is given in section 3, whereafter section four describes the analysis. The final results are discussed in section 5, followed by a conclusion and suggestions for future research in section 6. Additional figures and results can be found in the appendices.

2. Theoretical background

Roughly all stars in our galaxy are formed in clusters, which is why they are particularly valuable to astronomers for modelling stellar evolution. These building blocks of the galaxy can be categorised into globular and open clusters. Globular clusters are tightly bound by gravity and are often found in the halo of galaxies. They may contain $\sim 10^5 - 10^6$ stars packed in spherical structures (Marr 2020). Open clusters, also known as galactic clusters, are located mostly in the arms of spiral- and irregular galaxies and contain $\lesssim 10^4$ stars (Portegies Zwart et al. 2001). Due to the loose gravitational bounds between individual stars in open clusters, the stellar mutual distances are larger than in globular clusters, making them comparably easy to observe. Whereas globular clusters are estimated to be 10-13 Gyr, open clusters have a typical age of < 1 Gyr. Hence, young clusters still contain massive stars which makes them an interesting target for researching stellar populations and cluster properties.

2.1. Open cluster formation and morphology

Star forming regions are formed when a giant cold molecular cloud collapses under its own gravity, as described by the Jeans instability (Jeans 1901). Different factors contribute to this violation of the cloud's initial equilibrium such as interactions with other clouds and shock waves emitted by supernovae. A combination of the cloud's pressure, turbulence, magnetic fields and moment of inertia withholds the interstellar cloud to collapse to form a single star (Larson 1985). Instead, multiple fragmented regions are formed from which individual stars are created. The universally accepted Stellar Initial Mass Function states that the proportion of higher and lower mass stars is usually the same no matter the region's size, environment or age.

As a young open cluster emerges from aforementioned star forming region, the initial size of such an open cluster is about the same as the collapsed molecular cloud. Nilakshi et al. (2002) studied the spatial structure and distribution of 38 open clusters by comparing the two main regions of an open cluster: the nuclear region, also known as the core, and halo region, referred to as the corona. It was found that the corona, with an average radius of 5.6 ± 1.9 pc, has similar structure as the core but is less dense. Typically, a higher number of massive stars are found in the core of an open cluster compared to its halo due to mass segregation. This process results from the dynamical evolution of the cluster, where massive stars sink to the cluster's centres whilst lighter members move away (Portegies Zwart et al. 2001). Consequently, the cluster's brightest stars are often visible near its core.

Initially, an open cluster advances through space as a group of stars, where its members have similar bulk motions. This distinguishes cluster member stars from other stars which we call field stars. Initially, the cluster's members are located near the birth region and diffuse over time due to gravitational interactions. This instability of open clusters is caused by their low total mass resulting in a higher constitution of the average star's velocity compared to cluster's escape velocity. Due to this stellar dispersion and the short lifespan of bright stars commonly found in the core, open clusters are typically known to exist no longer than 1 billion years. Albeit the relatively short lifetime of open clusters, they are interesting celestial bodies to scrutinise because when observed, their members are still young and have not totally scattered away from their origin yet. Resultantly, one can consider the stars within the cluster to have similar distances from an Earth's observer. When an open cluster is clearly visible it can be therefore be assumed to still be in the early stage of dynamical evolution.

2.2. Stellar evolution and zero age main sequence

A star goes through three main phases during its lifetime: the protostellar phase, the main sequence phase and the post-main sequence phase.

Once a protostar has contracted sufficiently to fuse hydrogen into helium in its core, it settles on the main sequence. In this stage of its existence, a star spends about 90% of its lifetime, until its core's main fuel consisting of hydrogen has been exhausted. Sequential to this main sequence phase, nuclear fusion ignites outside the core. During this hydrogen shell burning phase, the star expands and moves off the main sequence into its post-main sequence phase (Fig. 1).

The energy production rate is determined by the mass of a star. A higher rate of nuclear fusion results in a high luminosity. In a cluster, massive stars will remain on the main sequence

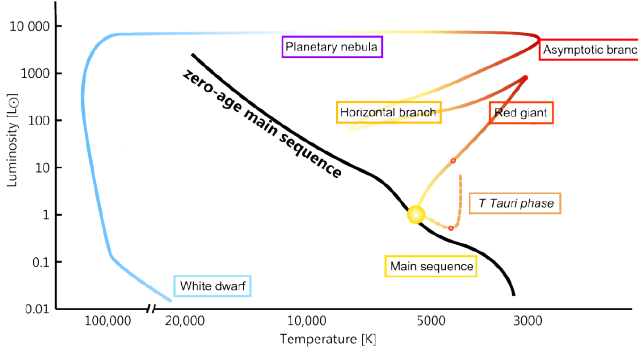


Fig. 1: The stellar evolution track of a solar mass star in the HR-diagram, taken from Wikimedia Commons (2014). After the protostellar phase, a star lands on the main sequence where it will stay for the majority of its lifetime. Its location on the main sequence depends on its mass. Once the star stops burning hydrogen in its core, it starts its post-main sequence phase. Finally, the star will evolve into a white dwarf.

shorter than lower mass stars as their core fuel depletes quicker, resulting the star to evolve off the main sequence more rapidly. The zero age main sequence (ZAMS) is a theoretical construct on which all age-zero stars appear once achieving conditions to start nuclear reactions in the core (see Fig. 1).

From the start of the 20th century, the Hertzsprung-Russell (HR) diagram by Hertzsprung (1908) and Russell (1914) has been used to depict the evolution of stars displaying a main sequence and post main sequence track, connected by a turnoff point (see Fig. 2). A star's location on an HR-diagram depends on the star's mass and the time that has elapsed since its initial cloud contraction. In an HR-diagram, the theoretical quantities luminosity L_\odot and surface temperature T_{eff} of the stars in a cluster are plotted against each other on a logarithmic scale. Since neither of these quantities are directly observable, colour indexes such as $B - V$ on the horizontal axis and apparent magnitude m_V on the vertical axis are often used instead. Such diagrams are named colour-magnitude diagrams (CMD).

2.3. Cluster membership and field stars

In the comprehensive study from Nilakshi et al. (2002) it was shown that an open cluster's corona consists of 75% of the cluster's members. Besides cluster members, there are also stars in the field of view that do not originate from the same molecular cloud as the open cluster. These are called field stars. When these stars are not excluded from the analysis, we speak of field star contamination. On average, this contamination amounts to $\sim 35\%$ for the core region and $\sim 80\%$ for the corona. One way to distinguish the field stars from the cluster's members is by studying their proper motion and parallaxes. Another way to decrease contamination by field stars is by solely studying the cluster's nuclear region, as the chance of encountering member stars here is higher compared to in the halo region. Lastly, foreground stars can be recognised by their dissociation from the main sequence on the HR-Diagram.

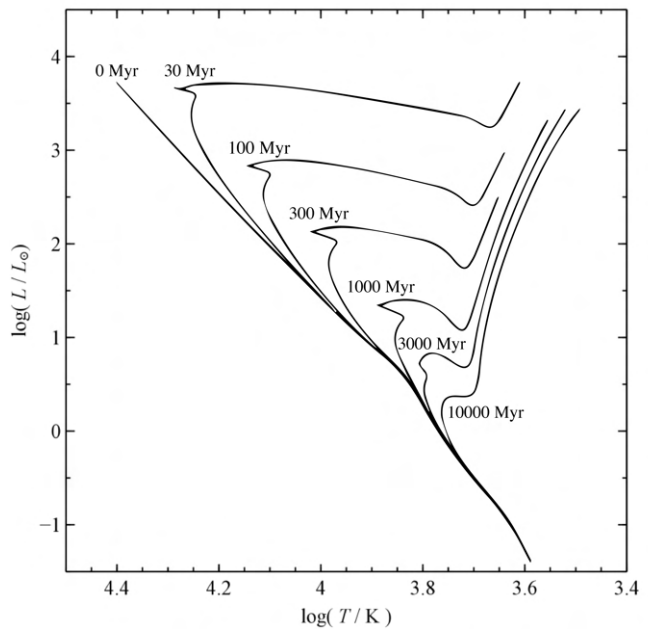


Fig. 2: Stellar isochrones from varying ages ranging from 0 to 10000 Myr. Every line illustrates a population of stars with masses ranging between $1M_\odot$ and $10M_\odot$. Young clusters have a high turnoff point corresponding to isochrones < 1000 Myr. Source image: <https://physics.stackexchange.com/users/4551/warrick>

2.4. Reddening and distance modulus

The difference between the apparent magnitude and a star's intrinsic magnitude is caused by the distance to the observer and interstellar extinction,

$$m_V - M_V = 5 \log d - 5 + A_V, \quad (1)$$

where m_V and M_V depict the apparent and absolute magnitude in the V-band, d the distance, and A_V the interstellar reddening in the photometric V-band. Extinction is caused by the scattering of light from dust clouds between the object and the observer.

Interstellar extinction has a wavelength dependency, causing shorter wavelengths to scatter more easily than longer wavelengths. As a result, a redder object is observed. By comparing the object's colour index $B - V$ to its intrinsic colour $(B - V)_0$, the degree of reddening $E(B - V)$ is calculated,

$$E(B - V) = (B - V) - (B - V)_0, \quad (2)$$

where $B - V$ is calculated by taking the difference of m_B and m_V . Since the extinction of the cluster's brightness A_V and reddening $E(B - V)$ are inextricably linked, their relation can be written as

$$\frac{A_V}{E(B - V)} = 3.2. \quad (3)$$

The 3.2 ratio is commonly used in similar studies.

2.5. Cluster age and turnoff point

The place on an HR-diagram where the brightest stars in a cluster start deviating from the main sequence is defined as the turnoff point. The location of the turnoff point reveals the age of a cluster. The presence of massive stars in a cluster leads to a high turnoff point in its CMD. Considering the rapid evolution of such stars, a high turnoff point implies that the cluster is young. On

the contrary, clusters with a low turnoff point imply antiquity. Using stellar evolution models for stars of various masses, stellar isochrones for varying ages can be constructed (see Fig. 2).

3. Observations

3.1. Target selection criteria

Criteria for the target selection were visual brightness, stellar density, and the age of the cluster. For the equipment used in this research, the limiting apparent magnitude is around 18 in the V-band for the used exposure times (see Fig. 5).

Although a high density of luminous stars in the cluster is preferred to obtain a sufficient amount of data for analysis, an extreme density such as in a globular cluster was undesirable. An excessive density of members prone source blending in the image, complicating photometry.

To facilitate age and distance estimations, a young open cluster is favourable due to the presence of massive stars positioned high up the cluster's main sequence.

Furthermore, the size and visibility of the target had to be taken into account to allow for sufficient data acquisition in one single observation run. For this research, visibility of an altitude of 30° above the horizon from the Anton Pannekoek Observatory between September and March was desirable.

3.1.1. The Double Cluster (NGC869 and NGC884)

The open clusters h and χ Persei, known as NGC869 and NGC884 respectively, meet all the previously mentioned criteria. These two clusters are bright, dense, and seemingly located near each other in the most northern part of the Perseus constellation and are visible from the lower latitudes in the Northern Hemisphere especially during autumn and winter nights. Therefore they are suitable and interesting stellar objects for the time frame of this research. According to Bragg and Kenyon (2005), the centres are located at $\alpha = 2^h18^m56^s \delta = +57^\circ8'2''$ and $\alpha = 2^h22^m4^s \delta = +57^\circ8'35''$ for h and χ Persei, respectively. Their angular distance thereby accounts to ~ 27 arcmin, leading to a total effective area of coverage of $\sim 0.6 \text{ deg}^2$ (Currie et al. 2010). Due to their small separation, they are often collectively referred to as 'the Double Cluster' or Caldwell 14. The high stellar density of bright stars in h and χ Persei indicate that the clusters are relatively young. With a total apparent magnitude of $m_V = 3.7$, the Double Cluster is a difficult object to observe by naked eye, but relatively simple to capture with binoculars.

Many researches on the Double Cluster are largely based on observational studies consisting of both spectroscopic and photometric procedures. Considering the limited time available for this research, photometric imaging techniques shall be enhanced with parallax data from the Gaia Data Release 3 to derive meaningful results (Collaboration et al. 2016; Brown et al. 2021).

3.1.2. Considerations for the Double Cluster (NGC869 and NGC884)

To be able to properly observe NGC869 and NGC884 individually, the angular separation of the two objects had to be large enough. Fortunately, by assessing the position of the Double Cluster from Earth's perspective, the cluster's main core regions did not seem to overlap.

The size of the area coverage of the Double Cluster also had to be taken into consideration. As discussed in section 2.1, the halo of an open cluster is around 5.6 ± 1.9 pc. Therefore, the

Double Cluster was divided into 4 separate imaging planes to include as many stars as possible in one observation run.

Lastly, due to the presence of bright stars, the ZAMS and turnoff point are easy to observe but require additional short exposures to avoid saturation.

3.2. Observing runs

Stellarium Planetarium Software was used to check for the cluster's visibility during all observing runs. Information on the observing runs is summarised in Table 1.

3.2.1. March 3rd 2021 at Rasjied's Observatory

The first observatory night took place in Amsterdam Zuidoost, The Netherlands, on March 3rd 2021 from 20:00 to 23:30, utilising a 235 mm Celestron C9.25 telescope at f/6.3 mounted on an Ipotron CEM25p with auto guiding capabilities. The imaging sensor was a ZWO ASI183MM CMOS with an 84% quantum efficiency peak and a pixel size of $2.4\mu\text{m}$, cooled to 1 degree. Using RGB broadband filters, useful data was composed to practice the first steps of photometry on. I observed this session remotely, since the telescope was operated by Rasjied Sloot at his private observatory. During this observing run only the Double Cluster was observed. Old calibration frames were used for data reduction.

3.2.2. April 16th 2021 at Anton Pannekoek Observatory, Small Dome

From April 16th 2021 20:00 to April 17th 2021 06:30, I performed an observational run at the Anton Pannekoek Observatory. This observatory is part of the Anton Pannekoek Institute of Astronomy and located in Amsterdam, The Netherlands. Data was accumulated from the open clusters NGC869, NGC884, NGC6811, NGC7209 and NGC6709 in the Johnson B, V, R filters. Utilising the ATIK460EX CCD camera with a 77% peak quantum efficiency and $4.54\mu\text{m}$ pixel size. Due to an optical misalignment of the 30cm Meade-Schmidt-Cassegrain telescope on a 10micron GM4000QCI mount, the majority of the images suffered from severe coma which made them unusable. This observational night was mainly useful for practising telescope operations.

3.2.3. June 13th 2021 at Anton Pannekoek Observatory, Big Dome

The final observations, on June 13th 2021 from 23:30 to 04:00, were also performed at the Anton Pannekoek Observatory, but now with the 50.8 cm Ritchey-Chrétien (RCOS) telescope on a 10micron GM4000QCI mount connected to a FLI Pro-line 16803 CCD Camera, cooled to a constant temperature of -20° C. The camera's peak quantum efficiency amounts to 64%, and its pixel size is $9\mu\text{m}$. Overall, the observing conditions were good with $\sim 1.7'' - 3.5''$ seeing and little to no clouds or satellites appearing in the field of sight. Employing 3 different broadband filters, the Johnson B, V, R filter, various exposure times were utilised adding up to a total integration time of over 2 hours, divided over four planes. For each plane 20 short exposure frames of 30 seconds in the B-band were taken. For both the V- and R-band, 10 short exposures were taken of 5 seconds, and 10 long exposures lasting 60 seconds. In order to collect sufficient data from the target object, it was important to capture enough cluster

Table 1: An overview of all observing runs carried out at three separate observatories. The objects and celestial coordinates of the centres of the frames are shown in the third and fourth column. The total integration time is given per filter in seconds. The average seeing was determined during the observations by analysing each individual frame through MaximDL. The final data used for this research was collected on 13/06/2021 at the big dome at the Anton Pannekoek Observatory, where the Double Cluster was observed in 4 separate frames (Fig. 3).

Date	Observatory	Object	Frame Centres	Integration time			Average seeing
				B	V	R	
03/03/2021	Rasjied's Observatory	NGC869	$\alpha = 02^h 18^m 56^s \delta = +57^\circ 08' 25''$	15x60s	15x60s	15x60s	2.5"
		NGC884	$\alpha = 02^h 22^m 04^s \delta = +57^\circ 08' 35''$	15x60s	15x60s	15x60s	2.5"
		NGC869&884 ¹	$\alpha = 35^h 08^m 17^s \delta = +57^\circ 07' 49''$	15x60s	15x60s	15x60s	2.5"
16/04/2021	APO Small dome	NGC869	$\alpha = 02^h 18^m 56^s \delta = +57^\circ 08' 25''$	10x60s, 11x8s	10x60s, 11x8s	10x60s, 11x8s	9.3" ²
		NGC884	$\alpha = 02^h 22^m 04^s \delta = +57^\circ 08' 35''$	10x60s, 10x8s	10x60s	18x60s	10"
		NGC6811	$\alpha = 19^h 37^m 18^s \delta = +46^\circ 23' 18''$	10x60s	10x60s	10x60s	8.7"
		NGC7209	$\alpha = 22^h 05^m 07^s \delta = +46^\circ 29' 01''$	10x60s	10x60s	10x60s	8.7"
		NGC6709	$\alpha = 18^h 51^m 18^s \delta = +10^\circ 19' 00''$	10x60s	10x60s	10x60s	7.5"
13/06/2021	APO Big dome	NGC869 top	$\alpha = 02^h 22^m 02^s \delta = +57^\circ 13' 06''$	20x30s	10x60s, 10x5s	10x60s, 10x5s	1.9"
		NGC869 bottom	$\alpha = 02^h 22^m 02^s \delta = +56^\circ 45' 58''$	20x30s	10x60s, 10x5s	10x60s, 10x5s	2.3"
		NGC884 top	$\alpha = 02^h 18^m 40^s \delta = +57^\circ 10' 50''$	20x30s	10x60s, 10x5s	10x60s, 10x5s	1.9"
		NGC884 bottom	$\alpha = 02^h 21^m 58^s \delta = +57^\circ 13' 06''$	20x30s	10x60s, 10x5s	10x60s, 10x5s	2"

¹ At Rasjied's Observatory, the Double Cluster was observed through three planes of which one was centred at the overlapping region of NGC869 and NGC884.

² The seeing from the observing run at the small dome depicted in the table does not represent the actual seeing. These values in the table are exceptionally high due to an optical misalignment of the telescope. This caused most images to suffer from severe coma.

members in one frame. A central star was chosen as a reference star present in all 4 frames. Considering the $30.42' \times 30.42'$ field of view from the telescope, the total observed area of the four planes covers $\sim 1 \text{ deg}^2$. Ultimately, only the data from this observing run has been used for the analysis of this research.

3.3. Data reduction

3.3.1. Pre-processing

The frames taken with the V filter showed a circular type of print near the edges of the images caused by damage on the filter's surface. Additionally, most long exposure images display an illumination gradient possibly originating from a light leak in the telescope's optical system (see Appendix A). The former issue was chiefly solved by the calibration frames, and the latter by background subtraction discussed in section 4.1.

Calibration was performed through the MaximDL software package, created by Cyanogen Imaging, using 10 flat frames for each filter, 10 dark frames for the 60 second exposures, and 20 dark frames for both the 30 and 5 second exposures. Moreover, 20 bias frames were used.

All individual frames were stacked per filter and exposure time in MaximDL through a sigma clipping combining method of the 16-bit integer fit files, where the sigma factor was set on 5.00. Black pixels were ignored and a linear normalisation was applied. The individual frames were aligned using an auto-correlation algorithm in MaximDL. Because of either bad focus or other disturbances in the image, one frame from NGC869 and six from NGC884 were excluded from stacking.

Overall, the observed data was reduced to 20 master frames: 5 frames for each plane, of which 1 medium exposure in the B filter, and a long and short exposure frame in both the R and V filter.

3.3.2. Plate solving

Every master frame was plate solved to obtain the RA and DEC sky coordinates of all sources. The plate solve was executed in

MaximDL using PinPoint and the USNO UCAC4 catalogue including stars up to magnitude 15. The uncertainty of the position measurement in the plate solve is approximated at 1 pixel accuracy (residual of $0.4''$).

Furthermore, the plate solve yielded a full width at half maximum (FWHM) value for every master frame. This information showed useful in the source detection step discussed in section 4.1.

4. Analysis

The aim of the analysis was to accurately fit both the cluster's main sequences and make subsequent comparisons with isochrones to derive at their distances and ages.

Through several steps of data processing, all observed sources from both clusters were added to a catalogue consisting of most importantly: a unique star ID, position, instrumental magnitude, and the related error. This catalogue was filtered on negative fluxes, low signal-to-noise ratio and duplicates. Subsequently, the sources (which could now be defined as stars) in the catalogue were selected based on their parallaxes and individual angular distances to each of the clusters' centres.

The last step of the analysis was to calculate the cluster's age and distance. Here, two main sequence fits were performed. The first fit was done without the enhancement of the Gaia data to estimate the distance. The second and final fit did include the Gaia enhancement, using these estimates.

I have written all the code for this research through the scientific open source environment Spyder, made available by the Anaconda Package Environment run by Python 3.7 (Raybaut 2009; ana 2020; Python Core Team 2019). At <https://github.com/Evameijling/BachelorProject.git> the source code for the following analysis can be found.

4.1. Data processing

The first processing procedure involved cropping the four master frames so any 0 value pixels would be excluded from the data. These pixels originated from the alignment of the individ-

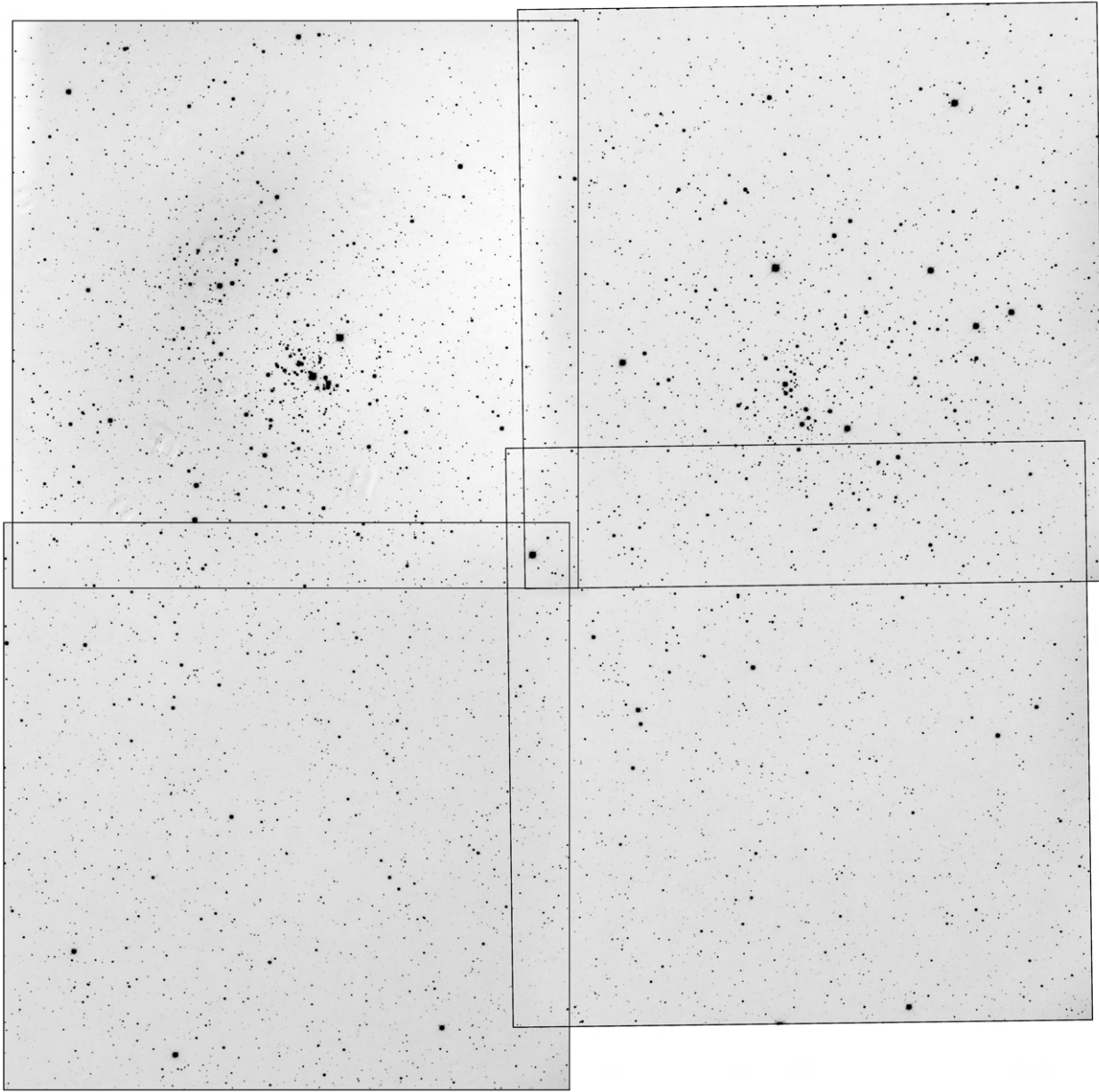


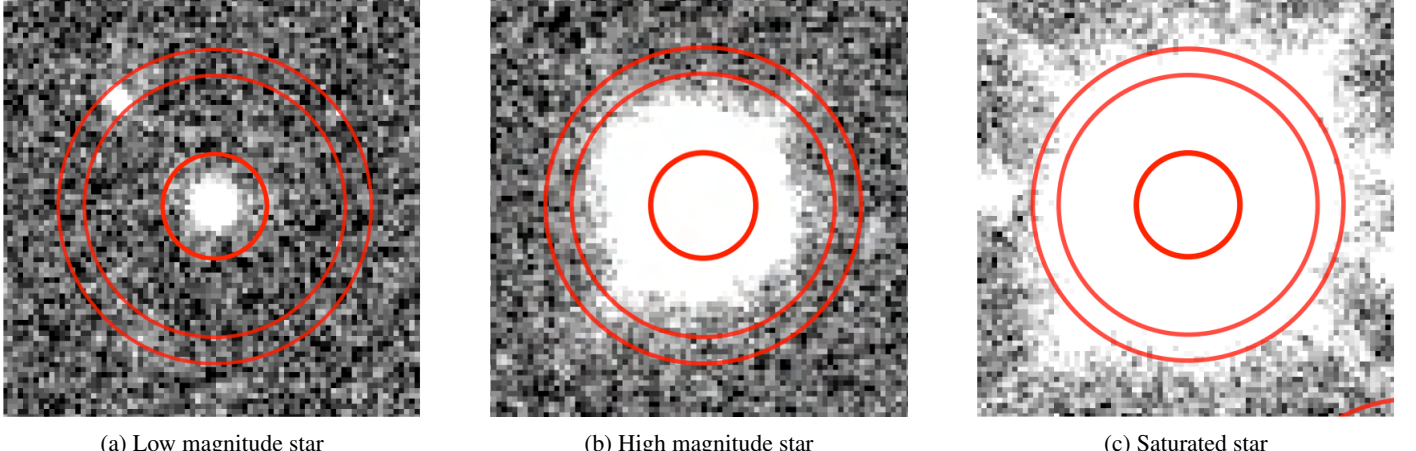
Fig. 3: Colour inverted mosaic of the four observed planes in the R-band. The two planes on the left capture NGC869 top and bottom. The two planes on the right show NGC884 top and bottom. Polar misalignment of the mount caused a slight field rotation during the observing run. The bright central star ($\alpha = 2^h20^m29^s$ $\delta = +56^\circ59'35''$) is visible in all four frames and was used as a reference point for pointing the telescope. The two dense core regions can be noticed in the two top planes. Because the brightest stars in this image are saturated, these stars were included in the catalogue using the short exposure measurements. The light leak caused by a malfunction in the telescope is visible in the top left frame.

ual frames to compose the master frame, where a slight difference in orientation of these individual frames causes the edges of the stacked frame to become zero valued. Utilising the Photutils package by Bradley et al. (2020), DAOStarFinder was applied for source detection on all four long exposure master frames in the R-band. Due to a very apparent light leak in the frames, this process was complicated, as the optimum value for the threshold and FWHM parameters strongly varied across the frames. Hence, a background subtraction was applied using the Photutils.background library to remove the light gradient from each frame, facilitating more accurate source detection (see Appendix 1). In order to detect as many sources as possible, whilst still

excluding noise that could mistakenly be identified as stars, a minimum threshold of 100 counts and FWHM of ten pixels was required. This estimate was determined through trial and error.

4.2. Aperture photometry

To generate stellar magnitudes from the detected sources, I used aperture photometry from the Photutils package. By setting an aperture radius appropriate for the majority of the detected sources, the flux is measured by integrating the pixel count within the aperture (see Fig. 4). The flux F measured in ADU, could then be converted to an instrumental magnitude m_{inst} , as



(a) Low magnitude star

(b) High magnitude star

(c) Saturated star

Fig. 4: Three examples of the aperture and annulus rings applied to stars of varying apparent brightnesses. The inner circle is called the aperture ring and measures the flux. The region between the outer two rings is called the annulus, and is used to determine the background. In (a) the flux of the star falls mostly within the aperture. Note that the annulus contains a star. For the aperture ring in (b) some of the flux falls outside the aperture ring, but still within the area of the inner annulus ring. Some stars such as (c) are saturated and therefore cannot be measured. For these stars the shorter exposures are needed.

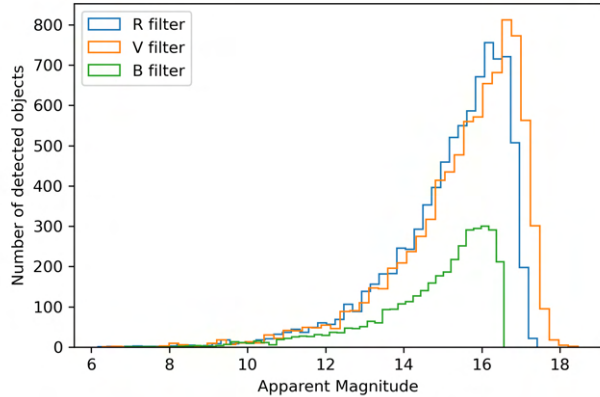


Fig. 5: The distribution of apparent magnitudes in the B-, V- and R-band of the stars in the filtered catalogue before the selection of stars based on position as described in section 4.3. The R- and V-band show a similar amount of detected objects, whereas the detection of the B-band is much lower due to a lower flux in this part of the stellar spectrum.

shown in equation 4:

$$m_{inst} = -2.5 \log_{10} F. \quad (4)$$

In these measurements of stellar flux, a certain degree of noise is included. By considering these various sources of noise, I was able to calculate the signal-to-noise (SNR) ratio for every source according to equation 5. In total, four sources contribute to the total noise of every photometric measurement of a source,

$$SNR = \frac{signal}{noise} = \frac{S_{object}}{(\sqrt{S_{object}} + n_{pixel}(S_{sky} + S_{dark} + R^2))}. \quad (5)$$

Sky background S_{sky} is caused by the detection of photoelectrons, and dark signal caused by electric currents S_{dark} is induced through thermally excited electrons. In equation 5, both these quantities represent the average pixel background value

found in the selected area from the photometric source. These are multiplied by the area of the aperture n_{pixel} to obtain the total contribution of noise within the aperture. An additional time-independent source of noise visible in equation 5 is the read out noise R^2 which depends on the electronics in the detector.

Since the read out noise from the FLI Pro-line 16803 CCD camera is $10e^-$, and the dark noise $0.005e^-$ per second (at $-30^\circ C$), these two noise sources are small compared to the sky background and can thus be excluded from the SNR calculation,

$$SNR = \frac{S_{object}}{\sqrt{S_{object} + n_{pix}(S_{sky})}}. \quad (6)$$

Looking at equation 6, we can find two limiting cases. We speak of the object limiting case when the signal is very high, making the noise contribution from the sky background comparably insignificant. In this case, equation 6 simplifies to $SNR = S_{object} / \sqrt{S_{object}}$. A background limiting case occurs for a very dim source where the background is dominant compared to the signal. For this case, equation 6 can be approximated with $SNR = S_{object} / \sqrt{n_{pix}(S_{sky})}$.

For a data set consisting of both bright and dim sources, we deal with both cases. Therefore, setting the aperture at an appropriate size for both types of stars is a crucial step in the photometric procedure. For a bright source with a high S_{object} , an oversized radius is tolerable, whereas for a dim source the SNR will quickly decrease. A smaller radius is therefore preferred, as the decline in SNR for the bright stars due to loss of flux measurement is less than the increase in SNR for dimmer stars (see Appendix B). Another advantage of choosing a smaller aperture radius is that there will be less overlapping apertures in the crowded regions.

I tested a series of aperture radii ranging from 7 to 20 pixels to compare their effect on the sources' flux and SNR (see Appendix B). Ultimately, I chose to adopt a radius size of 10 pixels which accounts for ± 2 times the FWHM. Creating a higher accuracy in the flux determination of the dimmer stars is preferable over the brightest stars because less uncertainty in the dimmer stars improves the main sequence fit (see section 4.6).

The error on the instrumental magnitude δm_{inst} only depends on the SNR given by equation 7,

Table 2: An overview of the operations performed on the catalogue containing the list of detected sources. The third column shows the length of the catalogue after each operation. The final 1222 stars in the catalogue are used for the final main sequence fit.

Operation on catalogue	Removed Stars	Stars in catalogue
Initial catalogue detected by starfinder	-	9762
Removing sources with negative flux	431	9331
Removing sources with SNR < 3 for V- and R-band	164	9167
Removing duplicate stars from overlapping planes	565	8602
Selecting stars based on Gaia parallaxes ¹	6840	1762
Selecting stars within 0.25° from cluster's centres	540	1222 ²

¹ This operation on the catalogue was based on the limiting distances of 2340 to 2635 pc for NGC869 and 2225 to 2475 pc for NGC884. These bounds were established through the first main sequence fit based on solely the observed data (without enhancement of Gaia Data).

² This number consists of 683 stars from NGC869 and 539 stars from NGC884.

$$\delta m_{inst} = 0.434 \frac{2.5}{SNR}. \quad (7)$$

This equation is obtained through standard error propagation using equation 4. From this equation the value of 0.434 follows, which equals $1/\ln(10)$.

For the photometry I decided to solely rely on local background subtraction from the found fluxes, as it would lead to more accurate results than a global background subtract. A global background subtract would yield an overestimated background value caused by the light leak (see Appendix A).

For every source, an annulus ring with an inner radius of 25 and outer radius of 30 pixels was applied to correct for the local background in the calculated flux in the aperture. To determine the background value within this annulus, the sigma clipped median is calculated to avoid overestimation caused when stars are present within the annulus (see Fig. 4a).

The instrumental magnitudes were calibrated to their corresponding apparent magnitudes using three reference stars for every plane. The reference magnitudes in the R-, V- and B-bands from these reference stars were found through Aladin Lite, adopting information from the SIMBAD Astronomical Database (Bonnarel et al. 2000; Wenger et al. 2000). The corresponding star from this research's catalogue was found through the program SAOImageDS9 (Joye and Mandel 2003).

4.3. Cleaning up initial data set

Through several filtering methods, sources with bad photometry caused by contamination from image artefacts or bad signal-to-noise ratio were removed from the initial catalogue. Similarly, stars with overlap from two or more planes were excluded. Ultimately, 1160 sources were filtered out from the initial source catalogue (see Table 2 and Fig. 6).

4.3.1. Filter long and short exposure times

As all planes were observed in both long and short exposures to correct for possible overexposure in the R- and V- band, every source in the catalogue possesses a double measurement in these two bands. The maximum pixel value in the aperture of each source was decisive for the selection of using either the short or long exposure magnitude values from the R- and V-band. Since the medium exposures in the B-band cause only one or two stars to be overexposed, no such filter step was applied here.

Above a pixel count of 50000, the linearity of the CCD sensor decreases. Hence, this value was taken as the lower bound

for overexposure above which stars are defined as unusable. Resultantly, 0.44% of the stars observed in the R filter, and 0.67% in the V filter were appointed the short exposure's instrumental magnitude, and its related error. The remaining sources were dimmer, and therefore linked to the long exposure values.

4.3.2. Filter on low SNR and duplicates from overlapping planes

For all stars in the catalogue, the lower bound value for SNR was set to 3. Accordingly, the chance that a located source was correctly identified as a star was near 100%. All sources below this 3σ SNR value were either removed (164 sources), or in the case of the B-band, reserved solely for CMDs using the tolerable V- and R-band magnitudes.

Another filtering step subject to the SNR value was the elimination of duplicate stars resulting from the overlap of two to four planes. In such an event, the star with the highest SNR value was selected, and the others were excluded from the catalogue. Eventually, 565 of such overlapping stars were excluded from the catalogue.

4.4. Position of measured stars

To establish an accurate main sequence fit of the cluster, field stars have to be excluded from the analysis. In this research, this was done by taking the angular distance of a star to the centre of the cluster and its distance to Earth into consideration.

A selection based on the position of the stars will fail to correctly identify all field stars within the cluster. One way to distinguish these stars from cluster members is through a thorough investigation in their kinematics, as shown in a research by Zhong et al. (2019). This, however, goes beyond the scope of this research.

4.4.1. Angular distance to cluster centre

The central point of each of the clusters was found by creating a heat map dependent on the stellar density (see Appendix C). From here on an 'angular distance to centre' value could be assigned for every star using the great circle distance calculation made possible by the astropy.units and astropy.coordinates library. This additional parameter has shown useful as a filter for creating CMDs. By an increasing angular distance to the centre, the probability that a star belongs to the cluster decreases. It is visible that stars which are located further away than 0.4 degrees from the centre seem to have very different locations in the CMD

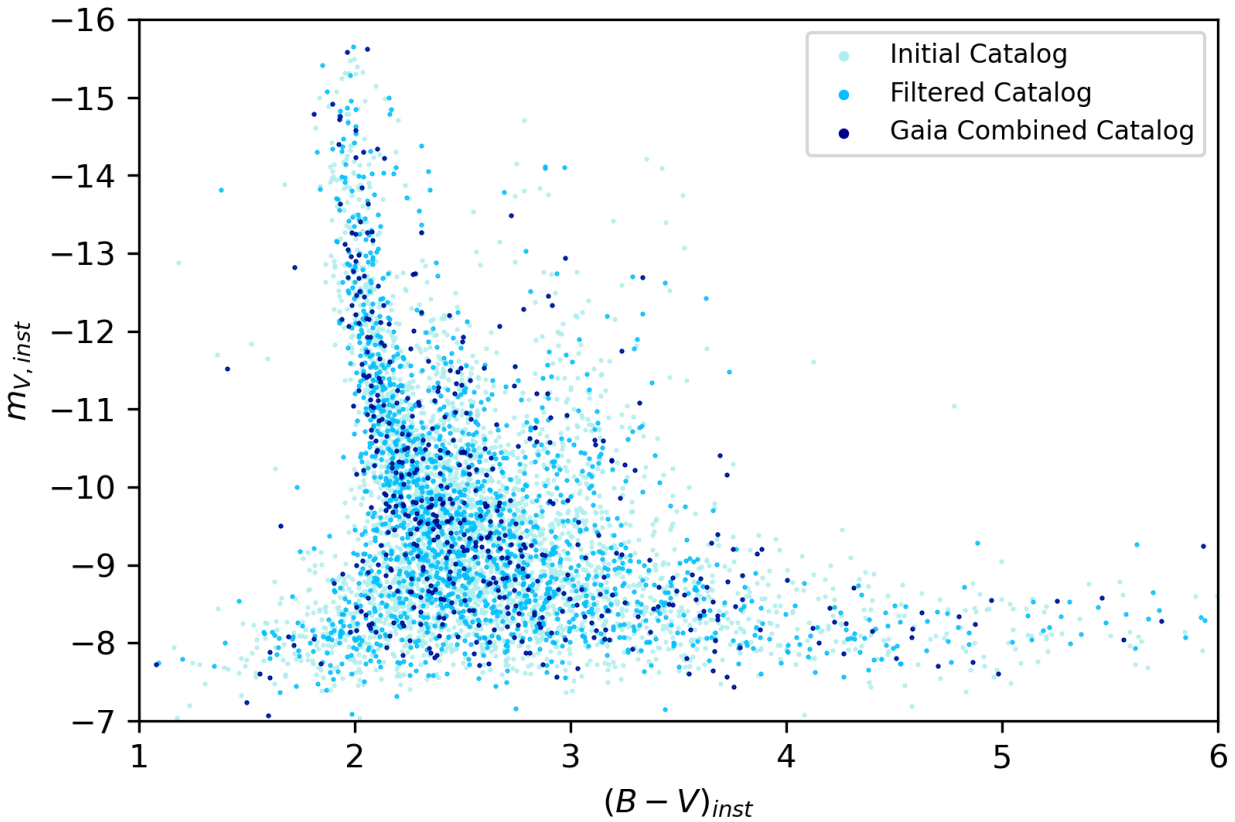


Fig. 6: Colour-magnitude diagram of NGC869 with the instrumental colour index $(B - V)_{inst}$ and apparent magnitude on the horizontal and vertical axes respectively. Note that these values are not calibrated yet. All sources included in the initial catalogue are shown in the lightest shade of blue. The residual of stars after removing stars with flux, with an SNR < 3 in the V- and R-band, and overlapping stars from planes, is shown in a slightly darker shade of blue. The scatter with the darkest shade of blue depict the stars within distances to Earth of 2340 - 2635 pc. These bounds were found through the first distance estimate based on all stars in the observed plane.

compared to the stars within 0.1 degrees from the centre, which form a well defined main sequence shape (Appendix C).

As Slesnick et al. (2002) state in their research, stars that are closest to the centre of the cluster are most likely to be members. Therefore, in this research, stars will consecutively be included from different radii from the cluster's core to see how it affects the CMDs (see Fig. 7a). By doing so, the contribution of the field star contamination is minimised whilst still including enough member stars to establish an accurate depiction of the main-sequence.

4.4.2. Distance to Earth

Data from the GAIA Data Release 3 was used to include the parallax of every star in the star catalogue. Operating a radius of 0.7 degrees from the central point in the overall observed data, 104066 stars were extracted from the database (see Fig. 7a). After selecting stars on their apparent brightness ($m_{GaiaG-band} < 17$) and correcting for a slight offset of -0.0057 in the RA direction, and +0.0029 in the DEC direction, 99.2% of the stars in my catalogue were matched with the Gaia data and appointed a parallax. Using equation 8, the distance to Earth d of these stars was gen-

erated from Gaia's parallax value p ,

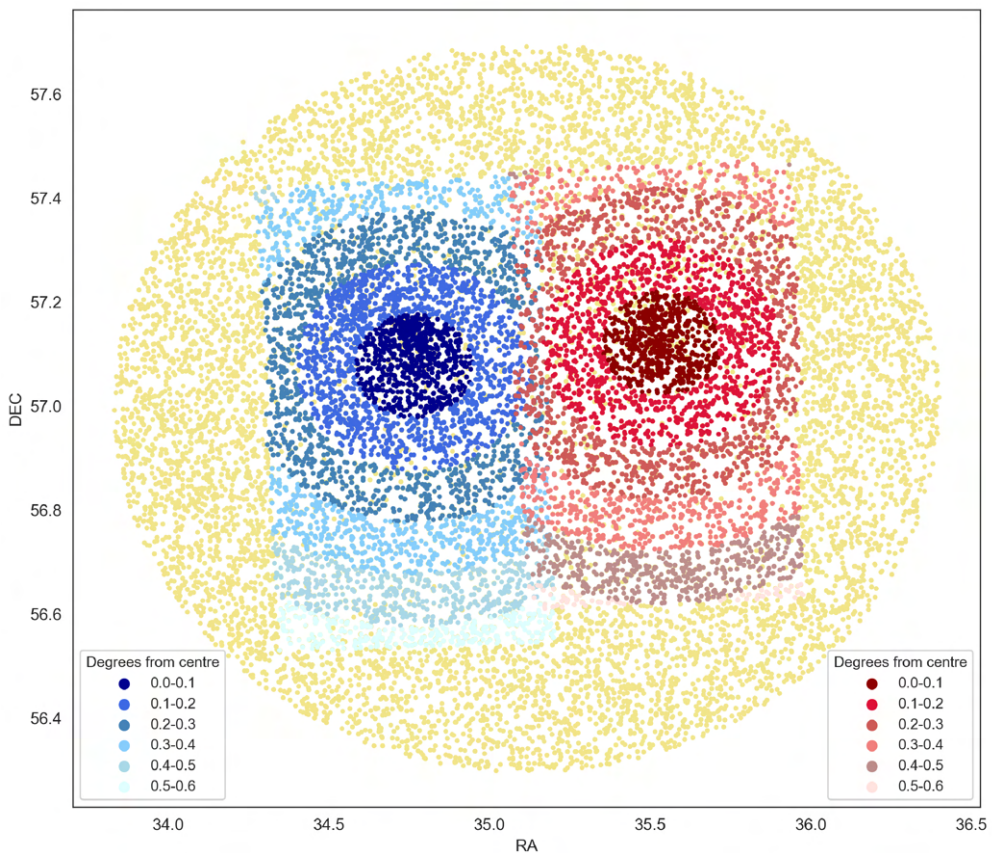
$$d = \frac{1}{p}, \quad (8)$$

where the distance is expressed in parsec, and the parallax in arcseconds.

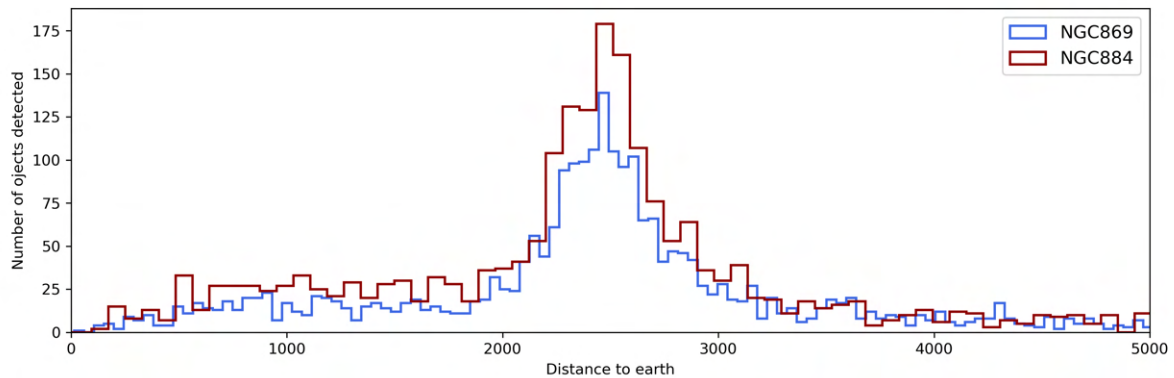
4.5. Main sequence fitting

To determine the distance and age of a cluster, the stellar population in the CMD needs to be fit to a stellar evolution model. The first step is to determine the cluster's extinction, dereddening and distance. Then, the turnoff point is determined which yields the age.

For this fit, I made a selection of stars based on their position as described in section 4.4. The maximum angular distance to each cluster's centre is set at 0.25° . This is roughly half the angular distance between the two clusters. Stars with a distance between 2340 - 2635 pc for NGC869, and 2225 - 2475 pc for NGC884 were included in the selection. These bounds were based on the first distance estimate and span wider than the average cluster size because of the uncertainties in the measured parallax. Ultimately, 683 and 539 stars were used for the final main sequence fit, for NGC869 and NGC884 respectively.



(a) Scatter plot of measured positions of the Double Cluster.



(b) A distance distribution histogram of NGC869 and NGC884.

Fig. 7: (a) shows the measured positions of the Double Cluster area on the sky. The planes obtained by observing NGC869 are depicted in different shades of blue. Similarly, NGC884 is shown in red. The yellow scatter points represent the positions of the stars found within 0.7 degrees from the centre by the GAIA Data Release 3. For every star in the catalogue, the corresponding star in the Gaia database is linked based on sky coordinates. (b) A distribution of the distance to Earth of all observed stars within 0.7 degrees from $\alpha = 02^{\text{h}}20^{\text{m}}29^{\text{s}}$ $\delta = +56^{\circ}59'34$. The distances are calculated using parallax measurements by GAIA Data Release 3. The majority of the stars are found in between 2-3 kpc from Earth. Since the cluster is located within this range, stars outside this range can be excluded as they are not part of the cluster.

4.5.1. Dereddening, extinction and distance

To determine the distance, the data has to be converted from apparent to absolute magnitude as described in equation 1.

The reddening value determined specifically for these clusters is assumed to be $E(B - V) = 0.55$ (Currie et al. 2010). From this value it follows that the interstellar extinction (A_V) is 1.76 (see equation 3).

The isochrones I used for this analysis were extracted from the CMD 3.6 input form web interface, obtaining the PARSEC evolutionary tracks by Bressan et al. (2012). As stated by Currie et al. (2010), the precise shape of these isochrones are partly determined by the metallicity of the individual cluster which influences the luminosity of different aged stars. Different metallicities lead to variations in the uncertainty of the distance modulus.

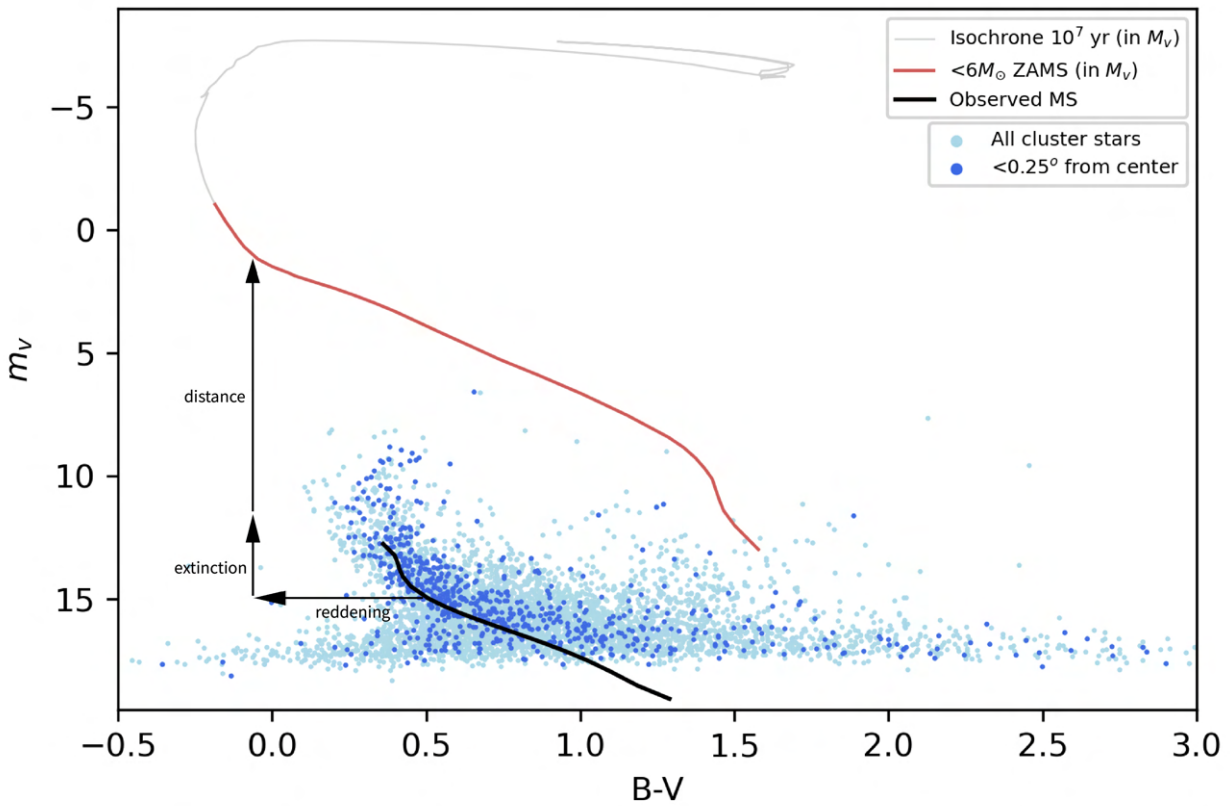


Fig. 8: Colour-magnitude diagram of NGC869 with the $B - V$ colour index and apparent magnitude on the horizontal and vertical axes respectively. Stars within 0.25° from the cluster's centre are shown in dark blue. The observed main sequence is depicted with a black line and is obtained through a least squares fitting method. The shape of this curve is approximated based on a theoretical isochrone with age 10^7 years and $M < 6M_\odot$. This theoretical isochrone is drawn in units of absolute magnitude, thus assuming a 10 pc distance and no interstellar extinction and reddening. Distance, interstellar extinction and reddening can be obtained by measuring the shift in the CMD from the observed MS position to the ZAMS as indicated by the arrows.

To date, there exists debate on the precise value of the metallicity of h and χ Per, ranging from a sub-solar metallicity of $Z = 0.01$ to a solar metallicity of $Z = 0.2$ (Currie et al. 2010). Considering the latter value has been employed by most recent studies, this research will adopt the solar variant for the post-zero-age main sequence tracks of $Z = 0.019$.

To fit the stellar population to its corresponding isochrone, an analytical function of the ZAMS is necessary. I have approximated this function with a fifth degree polynomial of the youngest isochrone in the data set for masses $M < 6M_\odot$ (see Fig. 8). This approximated function is fit on the most well defined part of the main sequence ($12 < m_V < 14$) based on the reduced χ^2 least square method, yielding the cluster's distance. The uncertainty on this distance is evaluated by calculating the minimum χ^2 value plus one. These resulting bounds have a 1σ error and are not symmetric.

4.5.2. Cluster age

To determine the age, the location of the turnoff point on the main sequence in the final CMD should be estimated. This is done by plotting several isochrones of different ages between 10 to 100 Myr (see Fig. 9). I have defined the age boundaries by eye,

by comparing the isochrones to the stars in the upper main sequence.

5. Results and discussion

Through this study I have successfully obtained photometric data for various open clusters and analysed them as shown in section 4. Additionally, astrometric data from the GAIA satellite was used for field star exclusion based on stellar parallaxes.

5.1. The distances to NGC869 and NGC884

For NGC869 a distance of 2565^{+85}_{-90} pc, and for NGC884 a distance of 2380^{+70}_{-75} pc has been found. The error estimations are based on a 1σ confidence interval. The distance between the clusters is 185 ± 110 pc, where the cluster NGC884 is closest to Earth. Taking into account the typical radius of a open clusters of 10 pc, it is not likely that the cluster's coronas have a overlapping region in space (Nilakshi et al. 2002). By excluding stars based on their distance to Earth which are most likely field stars, the main sequence becomes more precisely defined (see Appendix G). This refinement reduces the uncertainty on the main sequence fit resulting in more accurate distance determi-

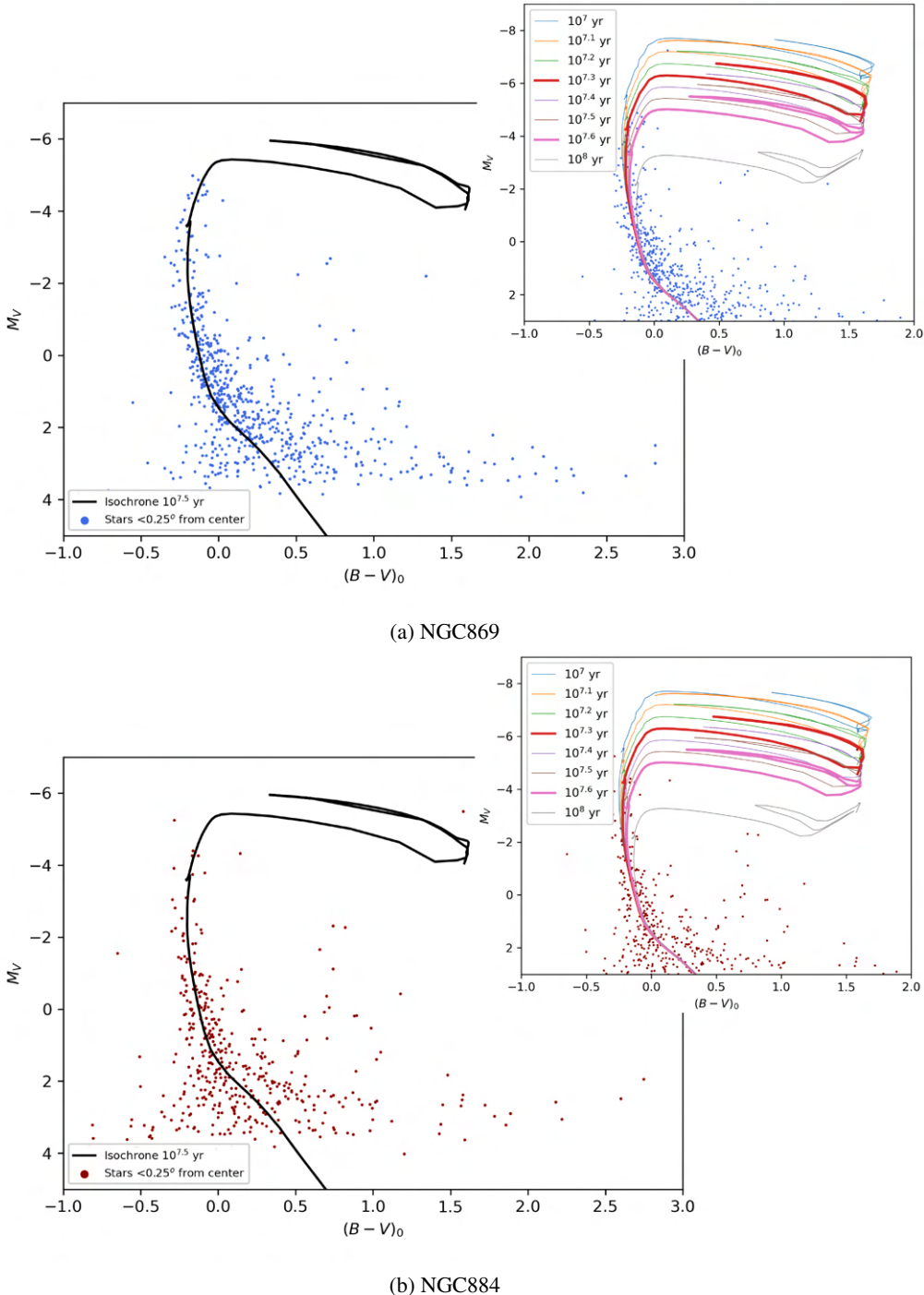


Fig. 9: Colour-magnitude diagram of NGC869 with the intrinsic B-V colour index and absolute magnitude on the horizontal and vertical axes respectively. The blue scatter represents the selection of stars based on their distance to Earth and within 0.25° of the cluster's centre. The best fit isochrone of these data points in the CMD is depicted with a black line. This isochrone represents a population of stars of the age 31 Myr and metallicity $Z = 0.019$. The coloured lines in the upper right figure display isochrones of ages between 10 to 100 Myr. The thick lines represent the boundaries for the age determination. The position of the data points in the CMD is based on a found distance of 2565^{+85}_{-90} pc and reddening $E(B - V)$ of 0.55.

nation. Without this reduced field star contamination, distances of 2495^{+140}_{-155} for NGC869 and 2360^{+115}_{-135} for NGC884 were found.

Field star contamination was reduced by excluding stars based on their parallax. This method could not exclude field stars located within the cluster. These stars can be identified by comparing their proper motion to the bulk proper motion of the cluster as demonstrated by Zhong et al. (2019).

When studying the locations of stars in the observed plane of both clusters, an unexpectedly high number of stars were found for distances ranging between 2000 and 3000 parsec. As stated by Currie et al. (2010), the halo population of the Double Cluster has a total diameter of ± 41 parsec. A possible explanation for this discrepancy is the location of the Double Cluster on the

Perseus arm in the Milky Way. This seems plausible as Wu et al. (2014) found the width of this spiral arm to be ~ 0.5 kpc.

5.2. The ages of NGC869 and NGC884

For both NGC869 and NGC884 ages of 20–40 Myr were found. The uncertainties of the findings are relatively large due to two main reasons. Firstly, there were not enough post main-sequence stars to strictly determine which isochrone describes the age of the clusters best. For example, one star in NGC869 is located on the 12.6 Myr isochrone. This suggests that the cluster could even be younger than 20 Myr (see Fig. 9).

Secondly, the ages were determined without any computational aids. Instead, they were determined by comparing the stars in the CMD with several isochrones ranging from 4–100 Myr by eye. In the studies conducted by Currie et al. (2010) and Slesnick et al. (2002), a mutual age of ~ 14 Myr was found for both clusters. Considering the uncertainties in my age determination, these values are in agreement with my results.

6. Conclusions

The present study was designed to determine the distance and age of the Double Cluster, consisting of the open clusters h and χ Persei. The data for this research was collected through photometric observations at the Anton Pannekoek Observatory. Additionally, Parallax measurements from the Gaia satellite were used to enhance the data set, inducing a more accurate reduction of field star contamination.

Although the ages of h and χ Persei were found to be in the same range, their mutual distance varies significantly. Therefore I establish that h and χ Persei are two separate clusters. Nevertheless, since molecular clouds larger than this distance exist, I conclude that that h and χ can originate from the same molecular cloud. This conclusion is in agreement with Slesnick et al. (2002).

So; are h and χ Persei siblings or strangers? Their significant mutual distance but similar ages suggests that the Double Cluster could be either. To determine whether we are looking at celestial twins born from the same molecular cloud, more accurate research on their existence is required.

6.1. Suggestions for future work

Despite the successful collection of data in this study, further work could be spent on increasing the accuracy of the measurements.

In the central regions of the clusters, the observed sources overlap. This leads to less accurate measurements of their instrumental magnitudes. PSF photometry could be a useful method to deal with the blending of sources in such crowded regions.

Whilst the current study was able to diminish the effects of the distorted data caused by the light leak in the telescope's optical system, a reproduction of this research without such deformities could also be fruitful for increasing the precision of the results.

Furthermore, the main sequence fit could be improved by increasing the total exposure time, as well as the amount of broadband filters used for the observations. This will improve the SNR values and establish a narrower range in the higher magnitude main sequence area. Utilising additional colour-colour and colour-magnitude diagrams, extra main sequence fits can be

made, decreasing the uncertainties on the determination of the cluster's age.

Lastly, further research could try to independently determine the reddening based on their observations.

Acknowledgements

I would like to express my deep appreciation to my supervisor Drs. M.R. Sloot for his valuable guidance and support. Without his help and encouragement this dissertation would have never been possible. I am grateful for S.C. Rodriguez Cedeño and my friends from Goes, for their faith and consolation in this difficult year of grief. Finally, I thank my family. Especially my father, Johannes Willem Gmelich Meijling. I will never forget his inexhaustible confidence and investment in me.

References

- (2020). Anaconda software distribution. *Anaconda Documentation*.
- Bailer-Jones, C. A. (2004). Microarcsecond astrometry with gaia: the solar system, the galaxy and beyond. *Proceedings of the International Astronomical Union*, 2004(IAUC196):429–443.
- Bonnarel, F., Fernique, P., Bienaymé, O., Egret, D., Genova, F., Louys, M., Ochsenbein, F., Wenger, M., and Bartlett, J. (2000). The aladin interactive sky atlas. a reference tool for identification of astronomical sources. *Astronomy and Astrophysics Supplement Series - ASTRON ASTROPHYS SUPPL SERIES*, 143:33–40.
- Bradley, L., Sipőcz, B., Robitaille, T., Tollerud, E., Vinícius, Z., Deil, C., Barbuy, K., Wilson, T. J., Busko, I., Günther, H. M., Cara, M., Conseil, S., Bostroem, A., Droetboom, M., Bray, E. M., Bratholm, L. A., Lim, P. L., Barentsen, G., Craig, M., Pascual, S., Perren, G., Greco, J., Donath, A., de Val-Borro, M., Kerzendorf, W., Bach, Y. P., Weaver, B. A., D'Eugenio, F., Souchereau, H., and Ferreira, L. (2020). astropy/photutils: 1.0.0.
- Bragg, A. E. and Kenyon, S. J. (2005). Structure and Mass Segregation in h and χ Persei. *AJ*, 130(1):134–147.
- Bressan, A., Marigo, P., Girardi, L., Salasnich, B., Dal Cero, C., Rubele, S., and Nanni, A. (2012). PARSEC: stellar tracks and isochrones with the PAOva and TRIeste Stellar Evolution Code. *MNRAS*, 427(1):127–145.
- Brown, A. G., Vallenari, A., Prusti, T., De Bruijne, J., Babusiaux, C., Biermann, M., Creevey, O., Evans, D., Eyer, L., Hutton, A., et al. (2021). Gaia early data release 3-summary of the contents and survey properties. *Astronomy & Astrophysics*, 649:A1.
- Collaboration, G. et al. (2016). The gaia mission. *arXiv preprint arXiv:1609.04153*.
- Currie, T., Hernandez, J., Irwin, J., Kenyon, S., Tokarz, S., Balog, Z., Bragg, A., Berlind, P., and Calkins, a. (2010). The stellar population of h and χ persei: Cluster properties, membership, and the intrinsic colors and temperatures of stars. *The Astrophysical Journal Supplement Series*, 186:191.
- Hertzsprung, E. (1908). Über die Sterne der Unterabteilungenc undac nach der Spektralklassifikation von Antonia C. Maury.
- Jeans, J. H. (1901). The Stability of a Spherical Nebula. [Abstract]. *Proceedings of the Royal Society of London Series I*, 68:454–455.
- Jones, A. R. (2020). Ptolemaic system.
- Joye, W. A. and Mandel, E. (2003). New Features of SAOImage DS9. In Payne, H. E., Jedrzejewski, R. I., and Hook, R. N., editors, *Astronomical Data Analysis Software and Systems XII*, volume 295 of *Astronomical Society of the Pacific Conference Series*, page 489.
- Larson, R. B. (1985). Cloud fragmentation and stellar masses. *MNRAS*, 214:379–398.
- Marr, J. H. (2020). The dynamics of globular clusters and elliptical galaxies.
- Nilakshi, Sagar, R., Pandey, A. K., and Mohan, V. (2002). A study of spatial structure of galactic open star clusters. *A&A*, 383:153–162.
- Portegies Zwart, S., McMillan, S., Hut, P., and Makino, J. (2001). Star cluster ecology - iv. dissection of an open star cluster: Photometry. *Monthly Notices of The Royal Astronomical Society - MON NOTIC ROY ASTRON SOC*, 321:199–226.
- Python Core Team (2019). *Python: A dynamic, open source programming language*. Python Software Foundation. Python version 3.7.
- Raybaut, P. (2009). Spyder. Available online at: pythonhosted.org.
- Russell, H. N. (1914). Relations Between the Spectra and Other Characteristics of the Stars. *Popular Astronomy*, 22:275–294.
- Slesnick, C. L., Hillenbrand, L. A., and Massey, P. (2002). The star formation history and mass function of the double cluster h and χ persei. *The Astrophysical Journal*, 576(2):880–893.
- Wenger, M., Ochsenbein, F., Egret, D., Dubois, P., Bonnarel, F., Borde, S., Genova, F., Jasniewicz, G., Laloë, S., Lesteven, S., and Monier, R. (2000). The SIMBAD astronomical database. The CDS reference database for astronomical objects. *A&AS*, 143:9–22.

Wikimedia Commons (2014). Evolution of solar-mass star on h-r diagram from

pre-ms phase to the end of fusion. File:Evolution of the Sun 2 EN.svg.

Wu, Y., Sato, M., Reid, M., Moscadelli, L., Zhang, B., Xu, Y., Brunthaler, A.,
Menten, K., Dame, T., and Zheng, X. (2014). Trigonometric parallaxes of
star-forming regions in the sagittarius spiral arm. *Astronomy & Astrophysics*,
566:A17.

Zhong, J., Chen, L., Kouwenhoven, M., Li, L., Shao, Z., and Hou, J. (2019).
Substructure and halo population of double cluster h and χ persei. *Astronomy
& Astrophysics*, 624.

Appendix A: Background subtraction and Starfinder

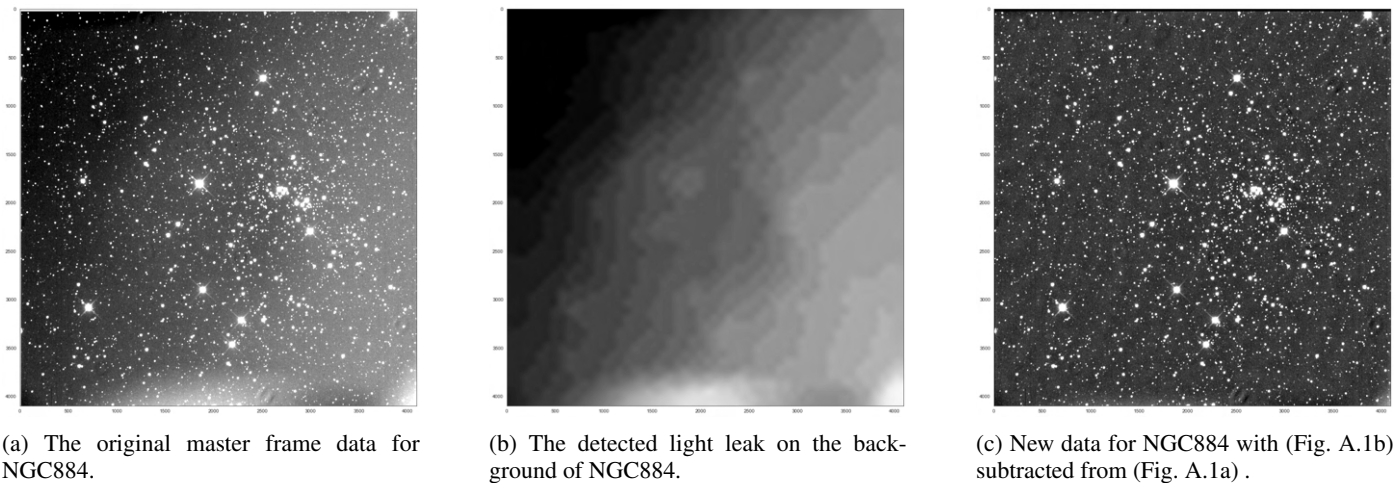


Fig. A.1: Removal of the light leak gradient through background subtraction.

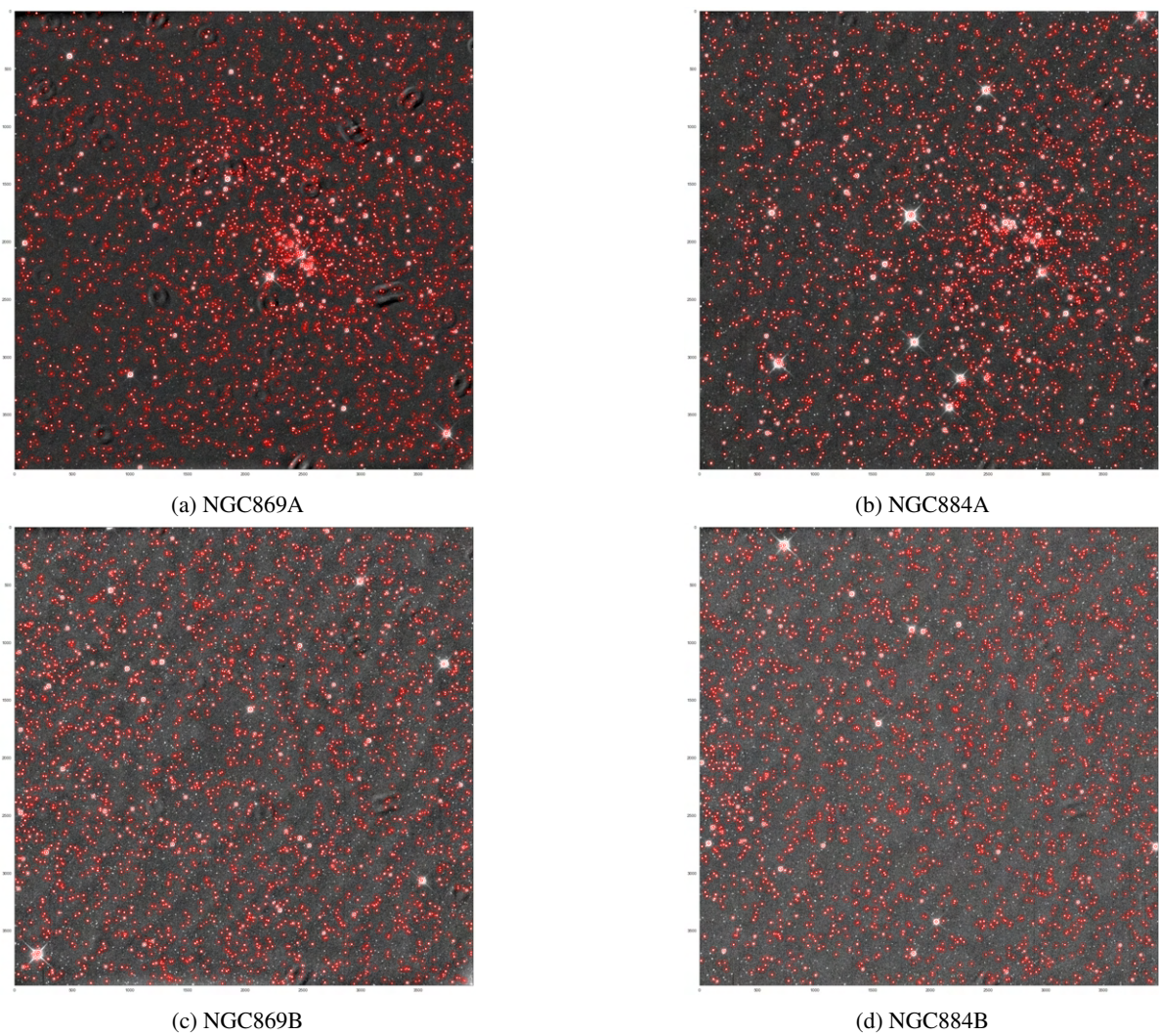
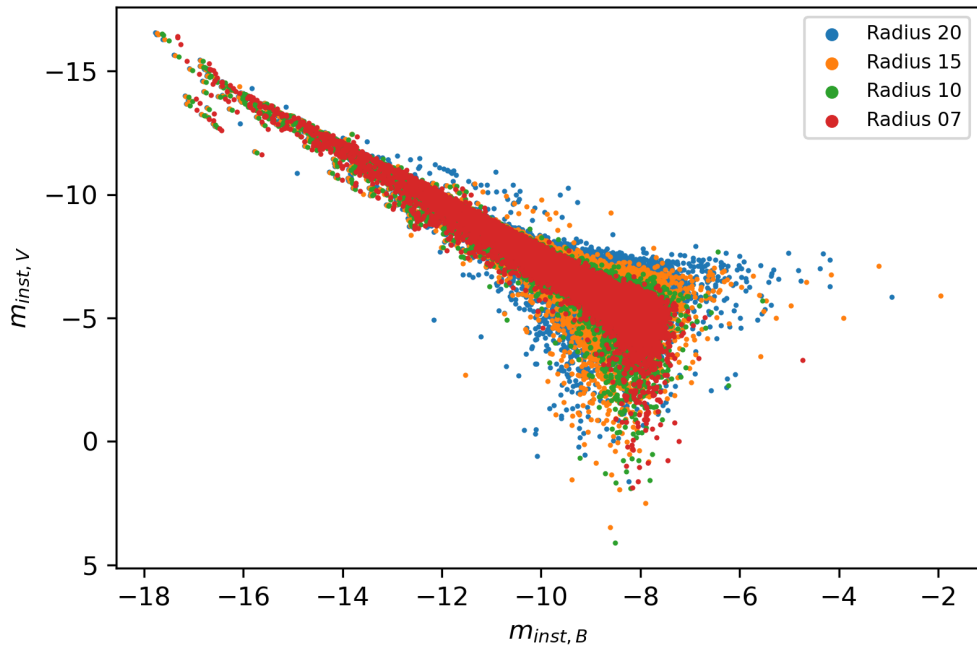
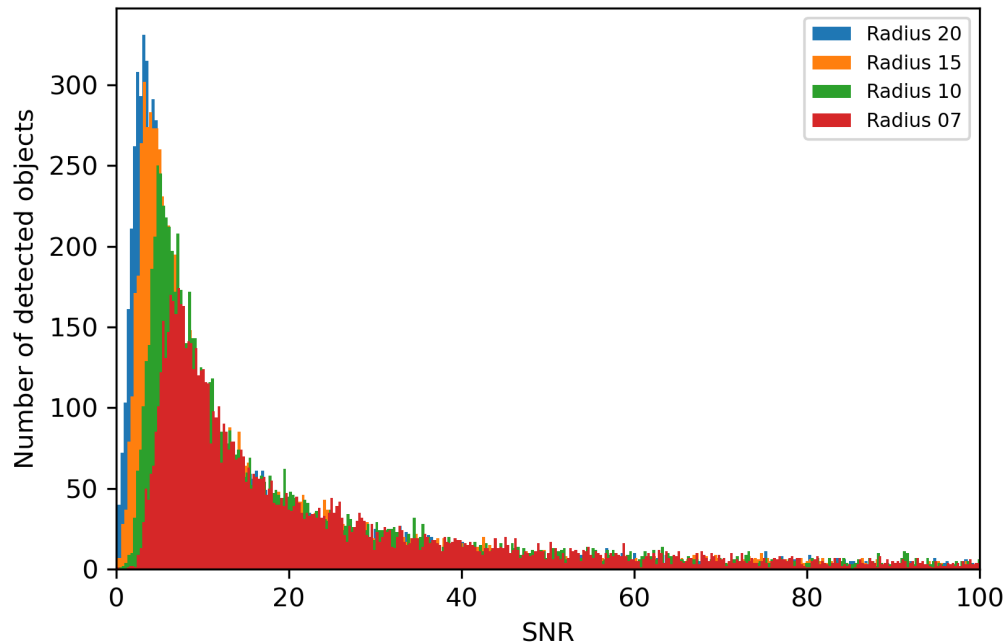


Fig. A.2: Stars detected by Starfinder.

Appendix B: Aperture photometry: aperture radius



(a) Magnitude-magnitude diagram for data with varying aperture radii.



(b) SNR distribution for varying aperture radii.

Fig. B.1: Aperture radii comparisons. By sacrificing some minor accuracy on the magnitude determination of bright stars caused by flux extending further than the aperture size, the flux of lower magnitude stars could be measured more precisely.

Appendix C: Determination of the cluster centre

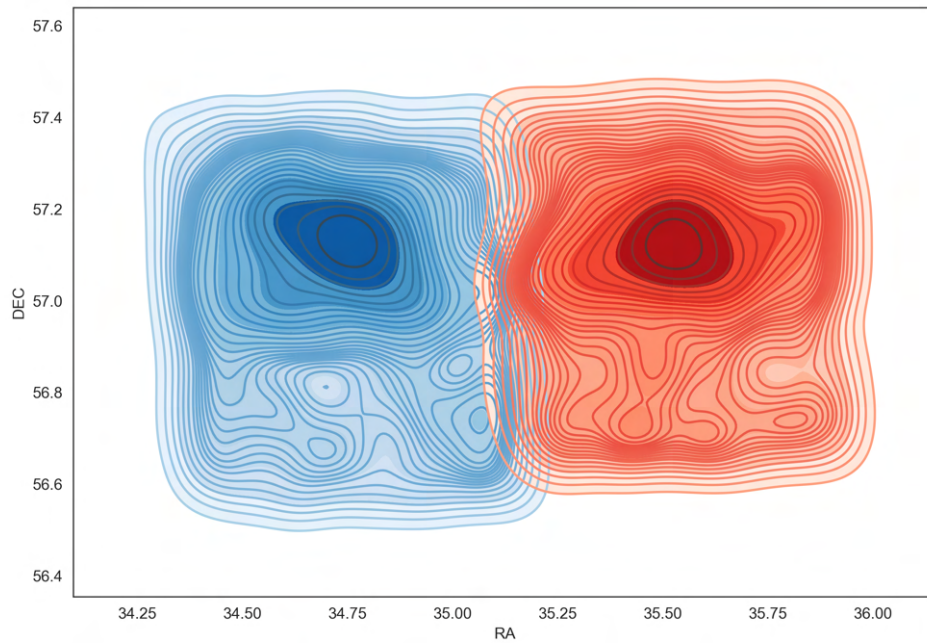
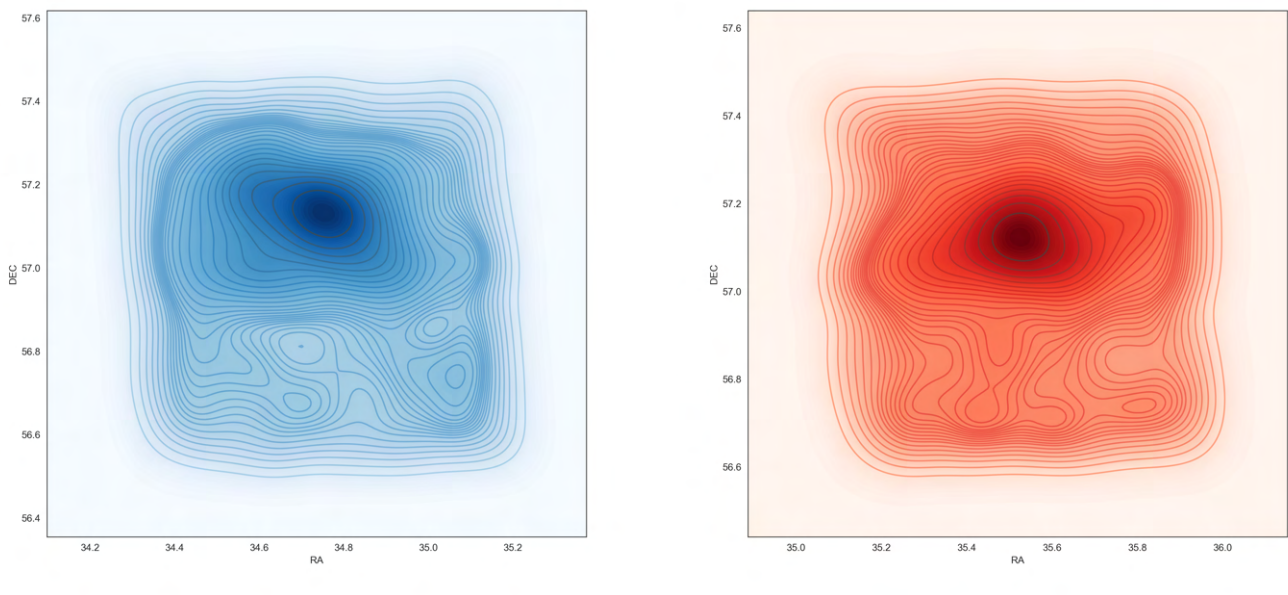


Fig. C.1: Heat Map of The Double Cluster



(a) NGC869

(b) NGC884

Fig. C.2: Heat maps of both clusters separately.

Appendix D: Core and halo population

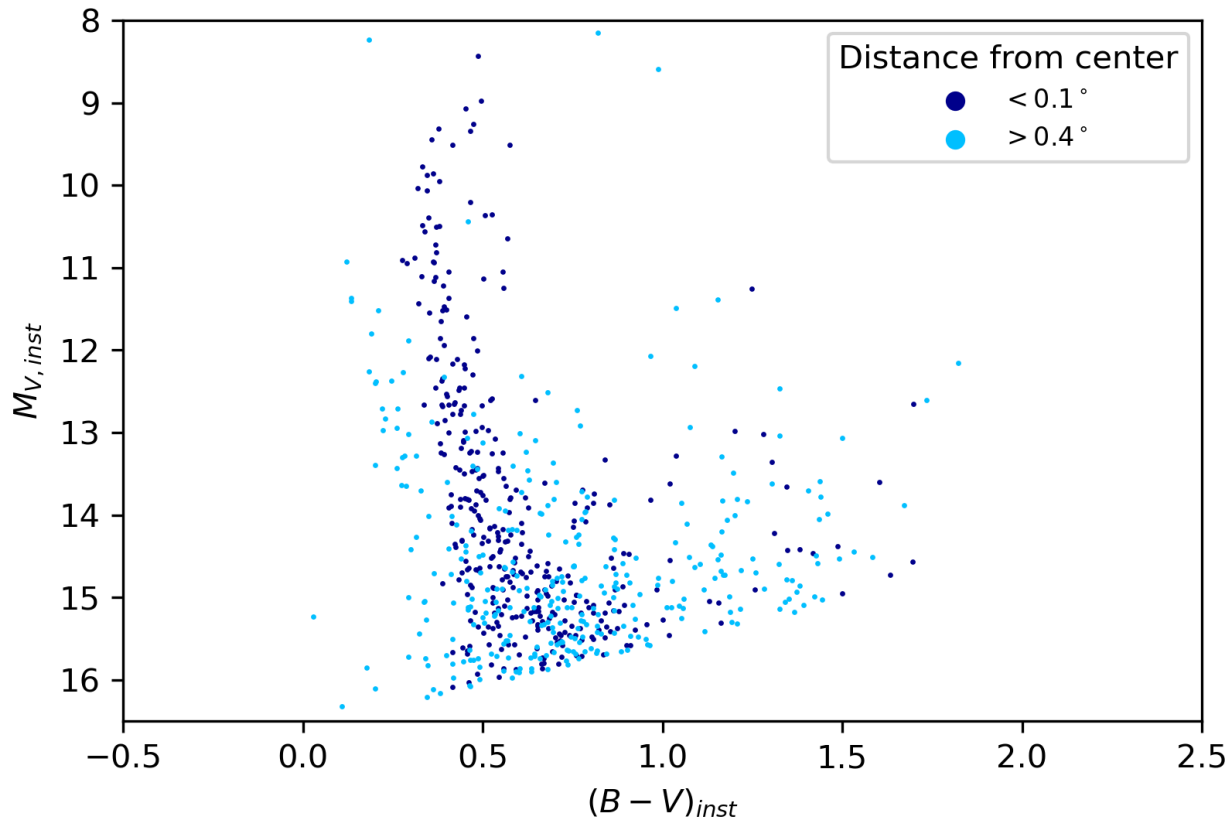


Fig. D.1: Comparison between stars near the centre ($< 0.1^\circ$) of the cluster and ($> 0.4^\circ$) from the centre. The stars in the core seem to have a better defined main sequence compared to the stars in the halo region.

Appendix E: 3D plot of the Double Cluster

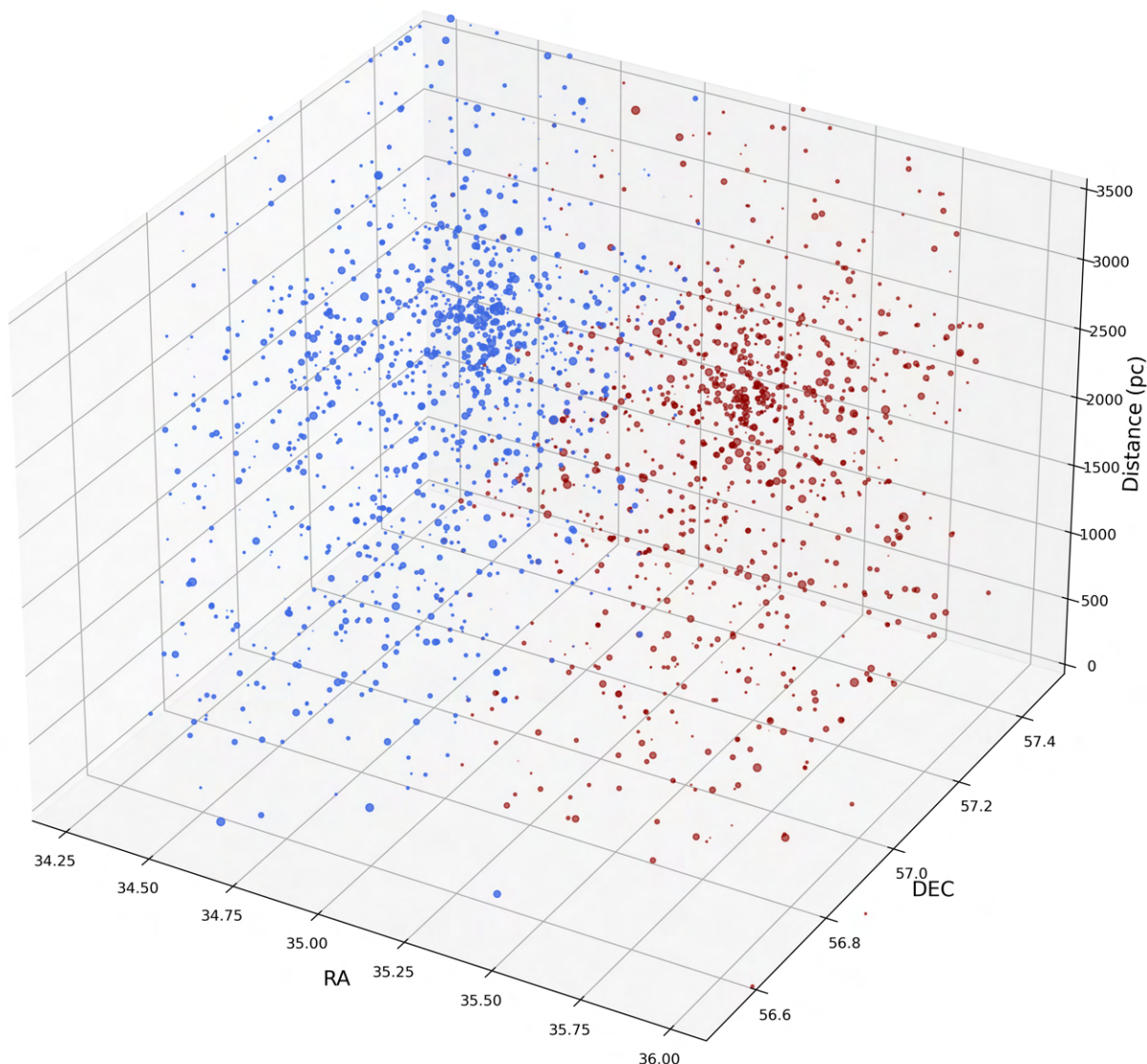
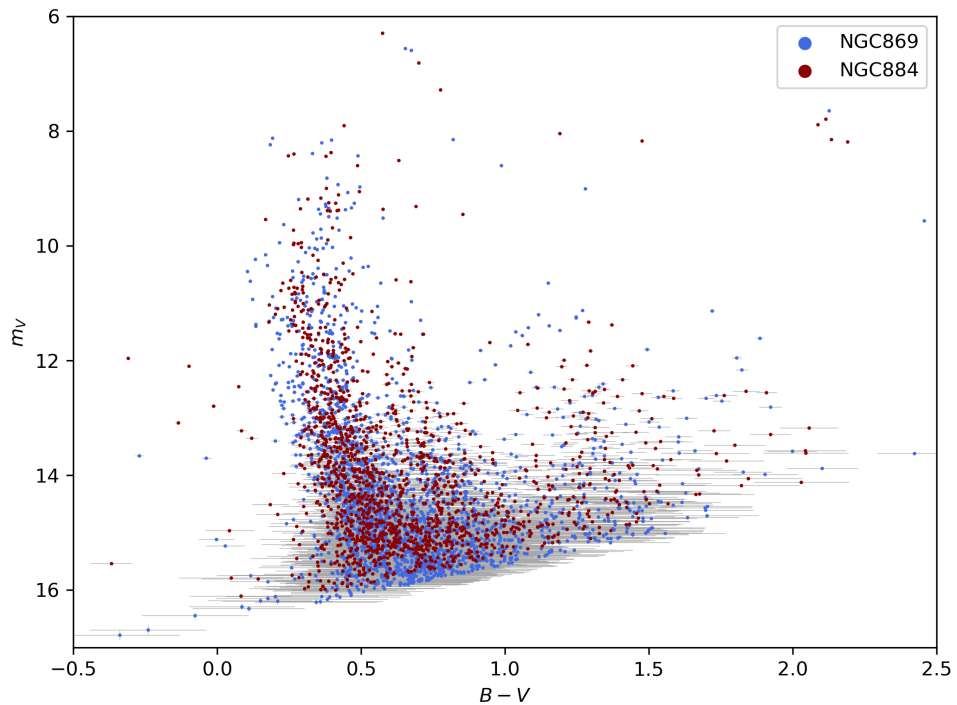
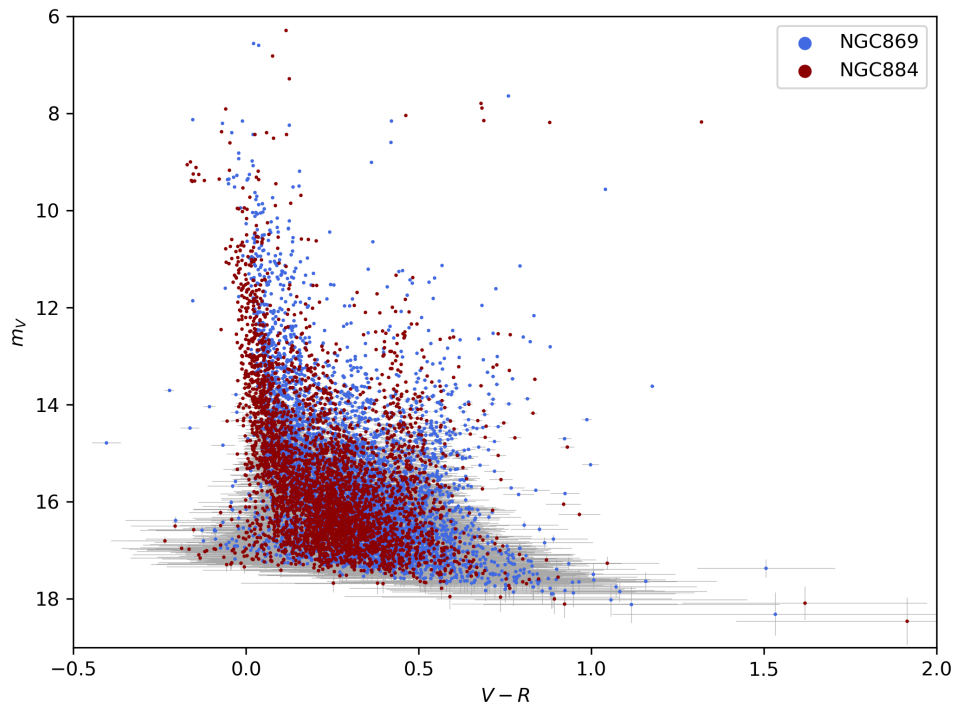


Fig. E.1: A 3D plot of the observed Double Cluster. NGC869 is shown in blue and NGC884 in red.

Appendix F: Colour-magnitude diagrams



(a) CMD for B-V with error bars



(b) CMD for V-R with error bars

Appendix G: CMDs without selection based on distance

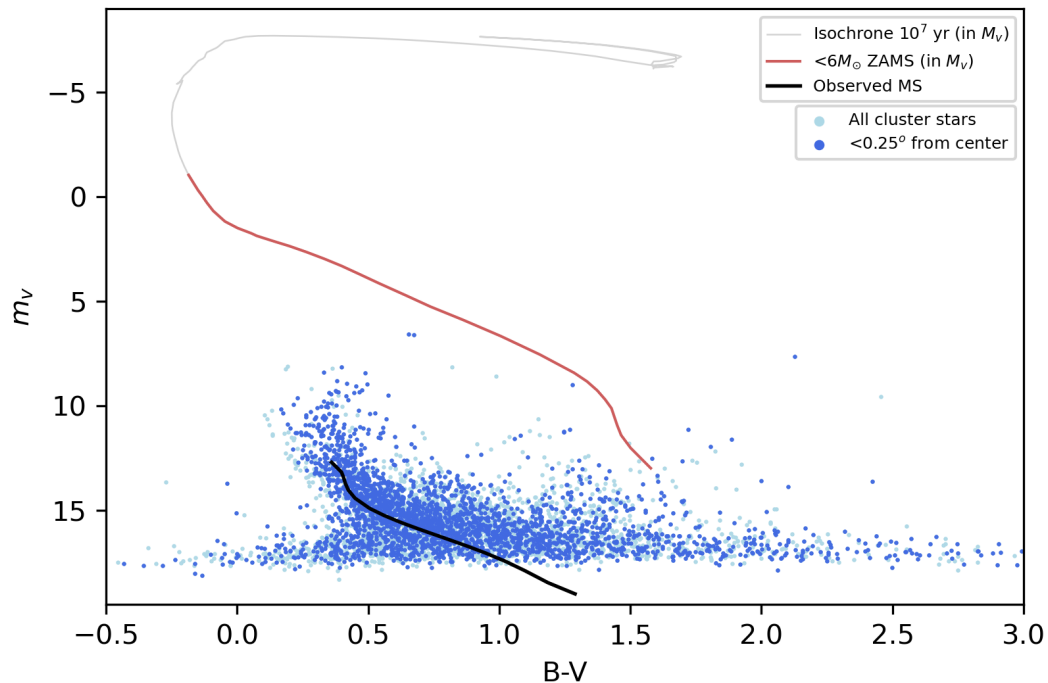


Fig. G.1: Similar result to Fig. 8 of NGC869 only without selection based on distance.

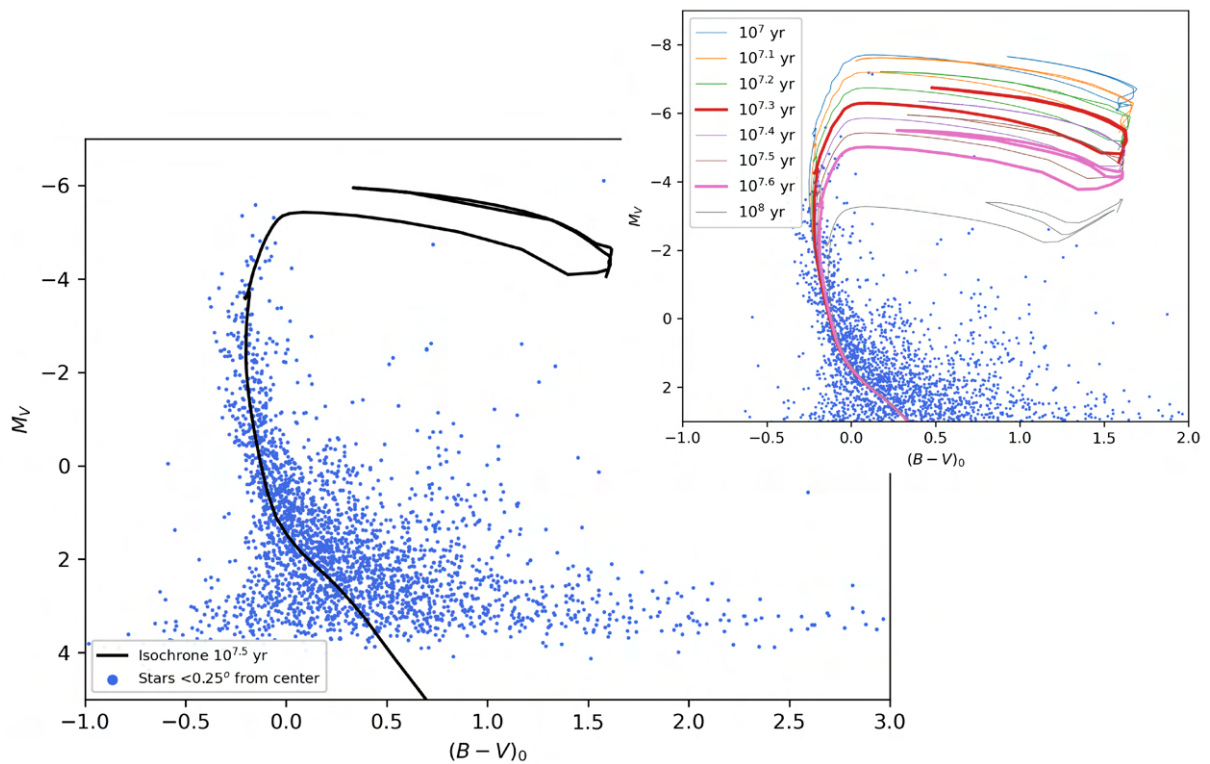


Fig. G.2: Similar result to Fig. 9 of NGC869 only without selection based on distance.

Appendix H: NGC884

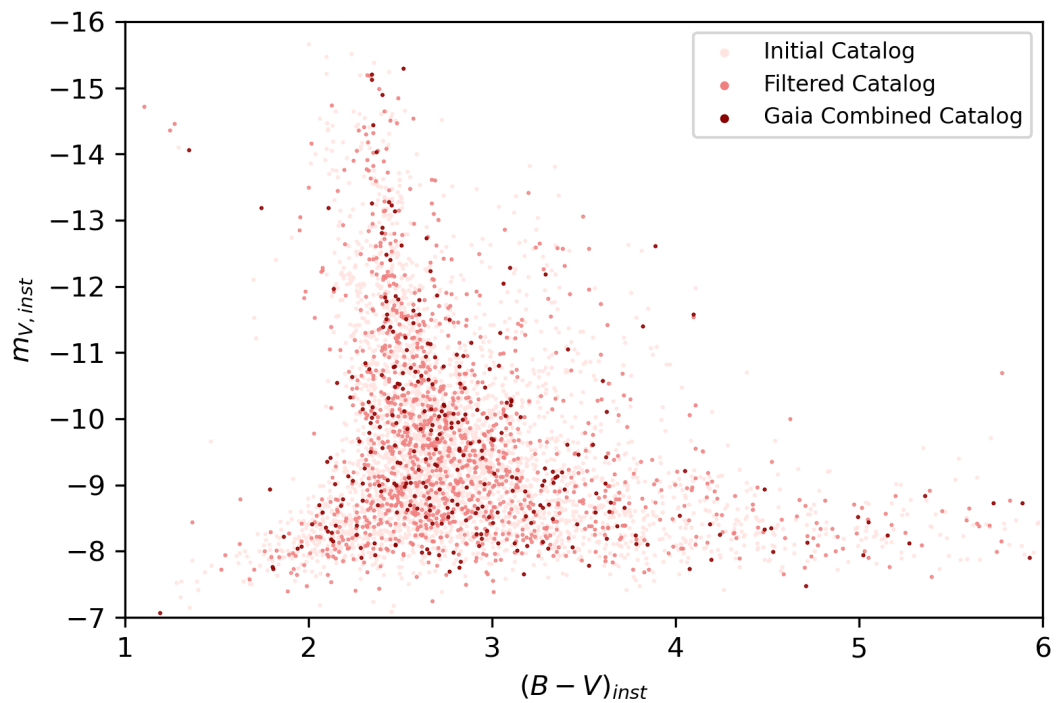


Fig. H.1: Similar result to Fig. 6 only now of NGC884.

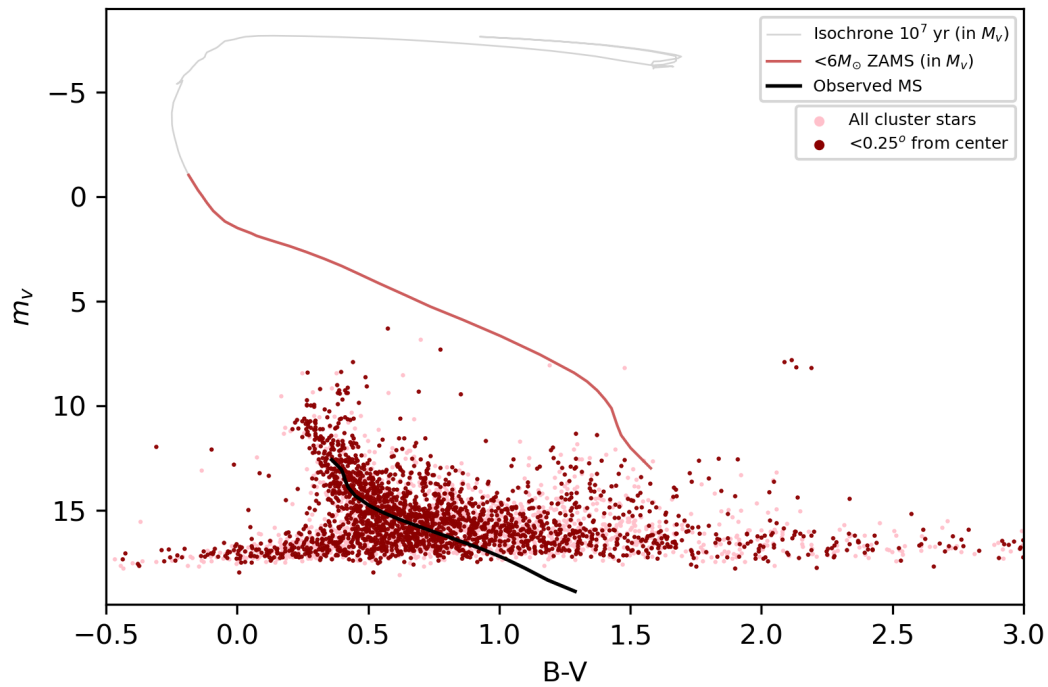


Fig. H.2: Similar result to Fig. 8 only now of NGC884 and without selection based on distance.

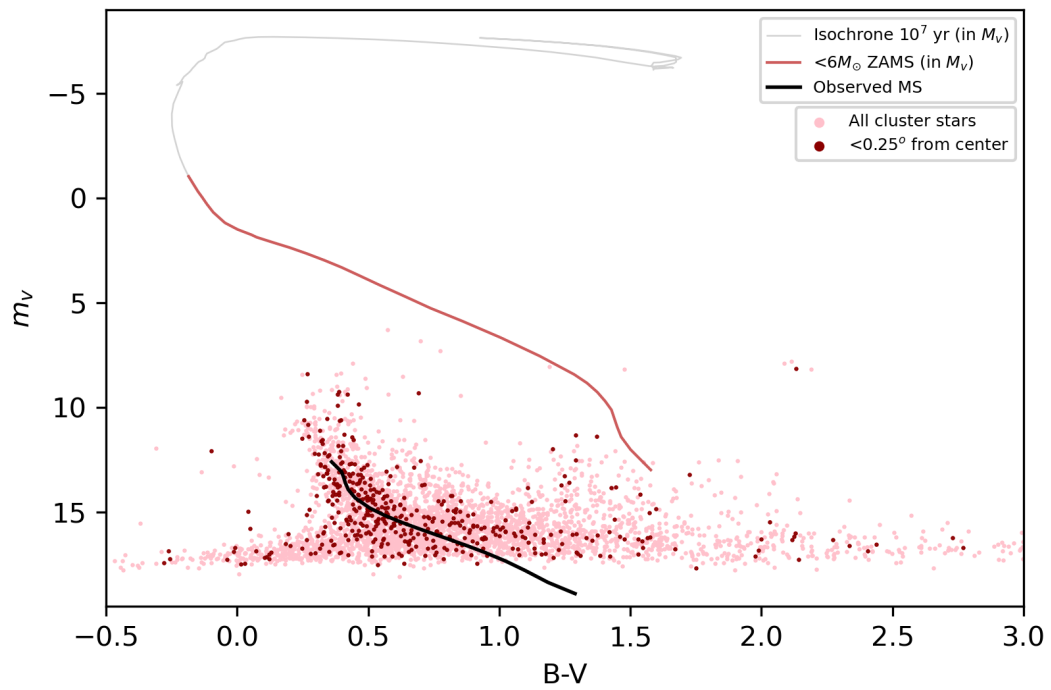


Fig. H.3: Similar result to Fig. 8 only now of NGC884.

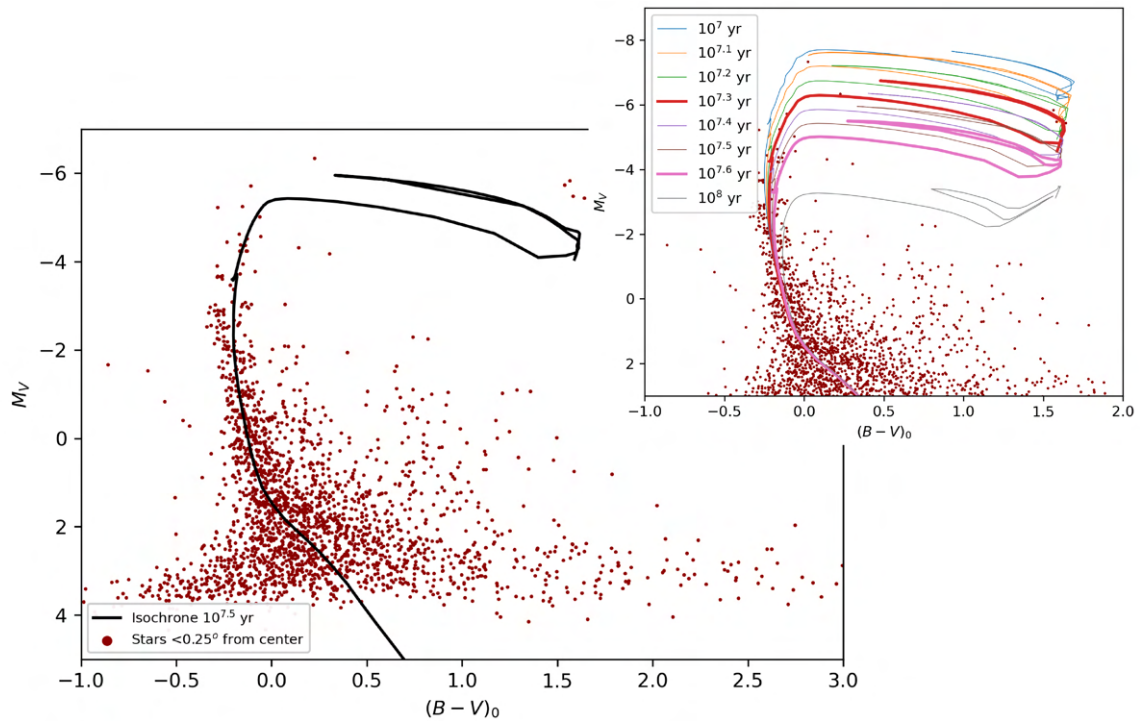


Fig. H.4: Similar result to Fig. 9 only now of NGC884 and without selection based on distance.

Appendix I: Observing logs

Time	Observations	Issues/remarks	Weather conditions/seeing
		16 graden gekoeld (door tijdsnood)	Heternaal helder!
20:48 – 20:50	10x V F ats	3s exposure	
20:55 – 20:57	10x R F ats	3s exposure	
20:00 – 21:02	10x B F ats	5s exposure	
21:11 – 21:15	20x Dark frames	3s exposure	
21:16 – 21:20	20x Dark frames	5s exposure	
21:30 – 22:30	Té scoop / schieten op Casse II voor scherstellen	Door middel van Banttinov masker grotere en scherper stellen: horizontale lijn moet door het midden van de ster zitten	
22:30 – 23:00	Té scoop / schieten op Dunne e Cluster	Blijbaar dat tussen de twee clusters te kijken waardoor ik de sterren niet kan herkennen	
23:00 – 23:05	NGC 869 Testing es R (checken op overbelichting etc.)		
23:05 – 23:15	NGC 869 Short exposures 8 sec		R filter: Gem. 14 pixels (FWHM) V filter: Gem. 16 pixels (FWHM) B filter: Gem. 9,5 pixels (FWHM)
23:15 – 23:45	NGC 869 Long exposures 60 sec		R filter: Gem. 13 pixels (FWHM) V filter: Gem. 15,5 pixels (FWHM) B filter: Gem. 13 pixels (FWHM)
00:20 – 00:30	NGC 884 Short exposures 8 sec		R filter: Gem. 14 pixels (FWHM) V filter: Gem. 16 pixels (FWHM) B filter: Gem. 11,5 pixels (FWHM)
00:40 – 01:10	NGC 884 Long exposures 60 sec	Foto's lijken een beetje uit focus (vaag omhoog) De camera stond niet meer aan toen ik terugkwam van pauze...	R filter: Gem. 15,2 pixels (FWHM) V filter: Gem. 18 pixels (FWHM) B filter: Gem. 13,5 pixels (FWHM)
01:10 – 01:30	Koffie pauze & Siern bellen & bijwerken opzoek		
01:30 – 02:20	Té scoop / schieten op Vega voor scherstellen (erst een andere geprobeerd (R filter)) Pasjed kwam kijken & helpen		
02:20 – 03:00	NGC 6811 Long exposures 60 sec	Bij R&V filter veel verschil in FWHM (waarschijnlijk doordat 1 deel in focus is, en rest minder erg) De linkerkant van de foto heeft betere FWHM dan rechts (links is dus meer in focus), opgegeven: 9 links & 17 rechts	R filter: Gem. 11,5 pixels (FWHM) V filter: Gem. 13 pixels (FWHM) B filter: Gem. 13 pixels (FWHM)
03:00 – 03:10	NGC 7209 zoeken & opnieuw beetje scherp gesteld		
03:15 – 03:50	NGC 7209 Long exposures 60 sec	Dto; voor R links 7,5 & rechts 16,8 Voor V links 9,3 & rechts 17 voor B links 7,5 & rechts 17,2	R filter: Gem. 12 pixels (FWHM) V filter: Gem. 13 pixels (FWHM) B filter: Gem. 12 pixels (FWHM)
03:50 – 04:00	Té scoop / schieten op HIP 86742 voor scherstellen (R filter)		
04:00 – 04:10	IC 4665 zoeken	Cluster te erg en een paar hele felle sterren, dus toch opzoek naar andere cluster dichtbij	
04:10 – 04:25	NGC 6709 zoeken & opnieuw scherstellen (zonder reference ster)		
04:25	NGC 6709 Long exposures 60 sec	Niet meer per se gelijke FWHM verdeling links en rechts Door 0004B zil vliegtug!	R filter: Gem. 10 pixels (FWHM) V filter: Gem. 9 pixels (FWHM) B filter: Gem. 13 pixels (FWHM)

Total word count:

....

Time	Observations	Issues/remarks	Weather conditions/seeing
		20 graden gekoeld (door tijdsnood) Zwarte vlek onder (was door filter die niet goed zit) TIPS: ideale volgorde filters flat field: BRV (want V filter laat veel meer licht door) idealtaal zo dicht mogelijk bij 50000 pixelwaarde! En lange exposure tijd Dark frames maken van elke gebruikte exposure tijd Checken of focusgetal bij verschiende filters anders is!	Heldermaal helder!
22:20	10x B filter	5s exposure	
	10x V filter	5s exposure Vreemde waas/veeg aan rechterkant van scherm Geen gelijk rond 40000 pixelwaarde	
	10x R filter	5s exposure Na 5s foto vliegt camera uit Grensgelijk op 26000 pixel waarde	
	10x I filter	10s exposure	
22:35		Kijken wat er mis is met de filters - gekke soort vel van op het V filter	
22:55		Kiezen welk object gaan observeren → duabel cluster 'verschillendste sterren en sterren in het centrum'	
23:15	Star at Cassiopeia (epsilon Cas) om telescoop goed te richten		
23:30	5 pers als focussster	Vee errors bij het focussen. Pakt steeds piek: 'pv ster' Focus vinden dmv L filter, 2 seconden 1 seconde exposure Computer opnieuw opgestart en toen werkte het wel goed → koeing naar 30 gecpan	
		Vuur afstel naar control room	
		22:20 22:29 22:56 22:59 22:35 ster als referentiester in alle 4 de frames	
00:30	NGC884_A (links boven) B filter medium exposure 20x 30s		B filter: Gem. 3° (FWHM)
	NGC884_A (links boven) V filter short exposure 10x 5s V filter long exposure 10x 60s	Camera uitgevallen na de 10s short exposure en 8s long exposure	V filter short: Gem. 1.8° (FWHM) V filter long: Gem. 1.7° (FWHM)
	NGC884_A (links boven) R filter shorts exposure 10x 5s R filter long exposure 10x 60s		R filter short: Gem. 2.5° (FWHM) R filter long: Gem. 2.5° (FWHM)
01:12	NGC884_B (links onder) B filter medium exposure 20x 30s		B filter: Gem. 3.5° (FWHM)
	NGC884_B (links onder) V filter short exposure 10x 5s V filter long exposure 10x 60s	Rechts beetje onder-kant zit een vage zwarte vlek aan de zijkant + strepen Camera uitgevallen na de 10s short exposure	V filter short: Gem. 1.8° (FWHM) V filter long: Gem. 2.2° (FWHM)
	NGC884_B (links boven) R filter shorts exposure 10x 5s R filter long exposure 10x 60s	Camera uitgevallen na de 1s en 4s long exposure	R filter short: Gem. 2.5° (FWHM) R filter long: Gem. 3° (FWHM)
02:00		Checken bij de camera of alles goed staat & focus Koepel iets naar oost verplaatst	
	NGC869_B (rechts onder) B filter medium exposure 20x 30s		B filter: Gem. 2.1° (FWHM)
	NGC869_B (rechts onder) V filter short exposure: 10x 5s V filter long exposure 10x 60s	Camera uitgevallen na de 4s long exposure	V filter short: Gem. 1.8° (FWHM) V filter long: Gem. 1.7° (FWHM)
	NGC869_B (rechts onder) R filter shorts exposure: 10x 5s R filter long exposure 10x 60s	Camera uitgevallen na 10s short exposure Nummering vanaf 5s voor gekf Camera uitgevallen na 6s long exposure	R filter short: Gem. 1.65° (FWHM) R filter long: Gem. 2° (FWHM)
		Rasjet naar huis	
02:57	NGC869_A (rechts boven) B filter medium exposure 20x 30s	Grote lens te klein door oude regen B filter begint met 0021 en eindigt met 0030, daarna valt camera uit Opnieuw begonnen want had naam verkeerd gegeven (B vs A)	B filter: Gem. 2.3° (FWHM)
	NGC869_A (rechts boven) V filter shorts exposure 10x 5s V filter long exposure 10x 60s	Camera uitgevallen na 6s long exposure	V filter short: Gem. 1.9° (FWHM) V filter long: Gem. 2.1° (FWHM)
	NGC869_A (rechts boven) R filter shorts exposure: 10x 5s R filter long exposure 10x 60s	Toe ing begint heel aan vanaf 0007 bij de R short en long exposures (loop tot 0016) Camera uitgevallen na 6s long exposure 0016 long heeft grote verticale lijn over foto's!!!	R filter short: Gem. 1.8° (FWHM) R filter long: Gem. 2° (FWHM)
		Snapjes maken & naam veranderen van NGC884_1(LB) naar twee aparte voor elke cluster	
		Telescoop veranderen en koepel checken	
	OPNIEUW NGC884_A (links boven)	Nog een keer omdat de FWHM (te) hoog was aan het begin van de nacht doordat nette licht was/object te laag aan de horizon	B filter: Gem. 2.6° (FWHM)

	B filter medium exposure 20x 30s	Camera A gevallen na 1' en 6" en 9" en 11" en 14" medium exposure Steeds grotere 'witte waas' in het midden!!	
	TOCH NIET OPNIEUW NGC884_B (links onder) B filter medium exposure 20x 30s	Het leek steeds juister te worden en de camera bleef maar niet focusen.	B filter: Gem. 2.3° (FWHM)
04:20	20x Bias frames	0s exposure (automatisch) Gewoon in de richting waar ik eindigde met NGC884_A. Goed zo?	
		Klaar boven gegroept om daar flat frames te maken. Telescoop rechts omhoog richting west-gouw. Er ging op een duur van iets meer dan een minuut een hard piepend geluid.	
04:44	10x V flat frames 10s	Rond 20000	
	10x R flat frames 10s	Rond 32000	
	10x B flat frames 10s	Rond 33000	
04:53	10x V flat frames 5s	Rond 45000	
	10x R flat frames 5s	Rond 43000	
	10x B flat frames 5s	Rond 40000	
05:08		Te excessieve gegever te oppervlak voor beg island Terug naar de contro room om dark frames te starten	
05:30	10x Dark frames	60s exposure	
	20x Dark frames	30s exposure	
	20x Dark frames	5s exposure	
06:00		Afsluiten en naar huis!	

